2009

Dissipative Quantum Transport Using the Pauli Master Equation

Bo Fu
University of Massachusetts Amherst

DISSIPATIVE QUANTUM TRANSPORT USING THE PAULI MASTER EQUATION

A Thesis Presented

by

BO FU

Submitted to the Graduate School of the
University of Massachusetts Amherst in partial fulfillment
of the requirements for the degree of

MASTER OF SCIENCE IN ELECTRICAL AND COMPUTER ENGINEERING

September 2009

Electrical and Computer Engineering

DISSIPATIVE QUANTUM TRANSPORT USING THE PAULI MASTER EQUATION

A Thesis Presented

by

BO FU

Approved as to style and content by:

Massimo (Max) V. Fischetti, Chair

Eric Polizzi, Member

Neal Anderson, Member

Christopher V. Hollot , Department Chair
Electrical and Computer Engineering

To my family

ACKNOWLEDGMENTS

First of all I would like to express my sincere gratitude to Prof. Max Fischetti, who has been my advisor since the beginning of my study. He provided me with many helpful suggestions, important advice and constant encouragement during the course of this work. This work would not have been possible without his support. I also wish to express my appreciation to Professor Eric Polizzi for many fruitful discussions and I learned many useful numerical techniques from his class ECE614. Special thanks are to Prof. Neal Anderson, for kindly serving as my thesis committee and providing valuable suggestions that improved the quality of this study.

ABSTRACT

DISSIPATIVE QUANTUM TRANSPORT USING THE PAULI MASTER EQUATION

SEPTEMBER 2009

BO FU

B.Sc., HUAZHONG UNIVERSITY OF SCIENCE OF TECHNOLOGY

M.S.E.C.E., UNIVERSITY OF MASSACHUSETTS AMHERST

Directed by: Professor Massimo (Max) V. Fischetti

On the way to develop a complete full-band quantum transport simulation using the Pauli Master Equation, we show our present results on 1D *n*-*i*-*n* resistors, 1D double barrier resonant tunneling diodes (DBRTD), and 2D double-gate field effect transistors (DGFETs) using a simplified parabolic, spherical effective-mass band-structure model accounting for nonpolar scattering with acoustic (elastic) and optical (inelastic) silicon-like phonons. We also consider the effect of point-like dopants on the access resistance of thin-body double gate devices.

TABLE OF CONTENTS

LIST OF FIGURES

Figure **Page**

CHAPTER 1

INTRODUCTION

1.1 Overview

As CMOS technology enters into nanoscale, quantum effects become dominant. Traditional device simulation based on the semiclassical Boltzmann Transport Equation (BTE) [24, 11, 8] can not reveal electrostatic properties correctly. Models totally relying on quantum mechanics are needed.

1.2 Simulation approaches

In order to study quantum transport, there are mainly three methods: Wigner functions (WF) [28, 9], Non-equilibrium Green Functions (NEGF) [23, 20, 4, 5] and the Pauli master equation (PME) [6, 7]. These approaches are all capable to handle quantum transport problems but from different perspectives. The moments of the WF result in quantum mechanical macroscopic models such as the density gradient model, effective potential approach and quantum hydrodynamic model. To appreciate the difference of PME and NEGF, we can simply look at the way they calculate the electron density in the quantum transport framework.

$$n = \int_0^\infty dE P_{local}(E) f_{FD}(E), \tag{1.1}$$

where $P_{local}(E) = P(E)|\Phi(E)|^2$ is the local density of state. In NEGF, the infinity integral is calculated by discretizing energy with a grid fine enough to simulate the continuous energy states existing in the thermodynamic equilibrium in the contacts.

NEGF also assumes that for any energy, the amplitude of the injected wave function is unit, so that the wave function should not be normalized in the device, leaving the fundamental meaning that wave function is a measure of probability. PME, on the other hand, strongly depends on the discretization of energy spectrum. Instead of integrating over continuous energy, it sums up the contribution of each standing modes over energy

$$n = \sum_{E} P(E) f_{FD}(E) |\Phi(E)|^2, \tag{1.2}$$

where wave function $\Phi(E)$ in this case must be normalized to the area of the device.

Regarding scattering, PME treats the traveling states as scattering states, applying Fermi's Golden rule to calculate the transition rates between different states. In NEGF there is no satisfactory method to include scattering efficiently, because a set of Dyson equations (an integral form of Schrödinger equation) which form a convenient starting point for the development of a perturbation expansion, have to be solved. People have tried phenomenological ways such as introducing Büttinger probes [1], which adds extra scattering energy term Σ_s to the retarded Green's function

$$G^R = [EI - H - \Sigma_1 - \Sigma_2 - \Sigma_s]^{-1}. \tag{1.3}$$

Recent Jin's work accounting electron-phonon scattering in the NEGF framework shows very promising results [13, 12].

In all, compared with the NEGF method, the PME promises a smaller computational cost when accounting for weak inelastic scattering processes. This work employs the PME and the purpose of this thesis is to present the ability of the PME in handling dissipative quantum simulations.

1.3 Outline of the Thesis

The thesis is organized as following. Chapter 2 presents about the physics formulation of the PME. Chapter 3 discusses its numerical implementation. Chapter 4 presents results regarding two simple 1D examples, n-i-n resistors and double barrier resonant tunneling diodes (DBRTD). Chapter 5 shows the results on non phase-breaking interactions and electron-phonon processes in assessing the quantum access resistance of thin-body double-gate field effect transistors (DGFETs). We draw the conclusion in Chapter 6.

CHAPTER 2

THEORY FORMULATION

When the active region of a device is smaller than the dephasing length of the electrons, off-diagonal elements of the density matrix can be ignored [26]. Following the standing wave decomposition method [6] [7] [17], scattering states are used as basis states on which the density matrix is represented in the presence of weak scattering. For an open system the PME can be written as:

$$\frac{\partial \rho_u}{\partial t} = \sum_v (W_{uv}\rho_v - W_{vu}\rho_u) + \left[\frac{\partial (f_u - \rho_u)}{\partial t}\right]_{res}, \tag{2.1}$$

where u and v are indices labeling scattering states. The first and second terms on the right hand side can be considered respectively as master and contact operators acting on the density matrix. The transition rate W_{uv} from v to u can be evaluated using Fermi golden rule:

$$W_{uv} = \frac{2\pi}{\hbar} | < u|H_{int}|v > |^2 \delta(E_u - E_v \pm \hbar\omega_q), \tag{2.2}$$

where H_{int} is the interaction Hamiltonian, E_u and E_v are the total energy for electrons in states u and v, while ω_q is either the phonon frequency or zero if the scattering process is elastic.

The PME can be solved employing a Monte Carlo (MC) algorithm [11, 8] in a way very similar to the case of the BTE, since the hard-to-treat collisional terms are left unchanged, the only difference being that in the PME the field driving term disappears thanks to its diagonalization in the scattering-state representation. The non-equilibrium electrostatics is obtained by solving the PME coupled with Schrödinger,

Poisson and current continuity equations at the contacts until self-consistency is reached [6].

CHAPTER 3

NUMERICAL IMPLEMENTATION

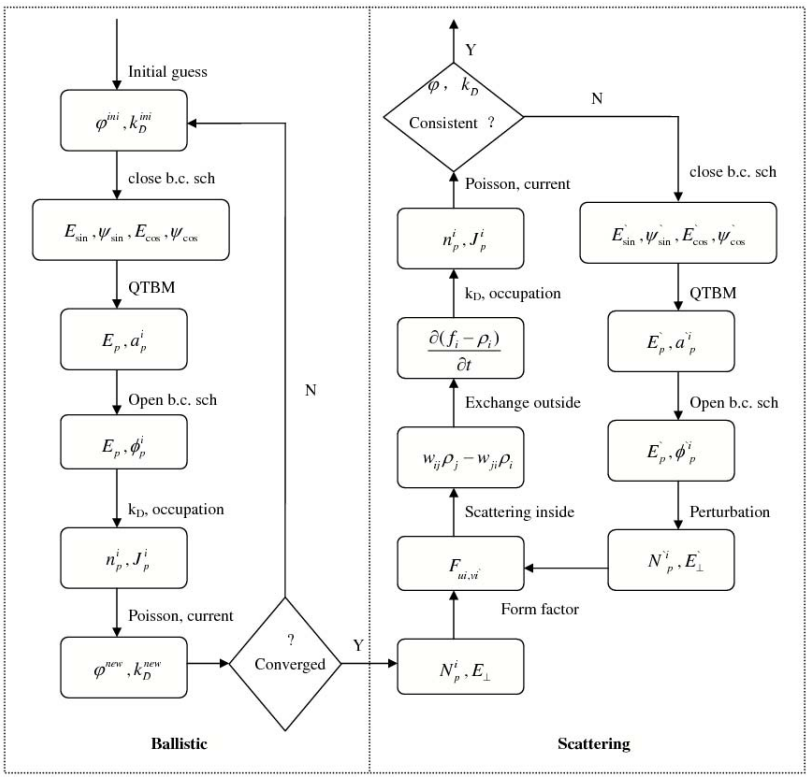

Figure 3.1. Flowchart of solving PME

The numerical implementation of PME can be divided into two main steps as shown in the flowchart of Fig. 3.1. First, we need to find self-consistent ballistic solution in the basis of scattering states and then in the second step, transitions of electrons (diagonal terms of density matrix) between different scattering states and with contacts are evaluated to include irreversible processes. Since the 2D case is conceptually similar to the 1D case except for the presence of evanescent waves when

considering traveling waves injected from contacts, the emphasis is placed on 1D. The differences will be discussed in 2D.

3.1 PME in 1D

3.1.1 Ballistic solution

The Master equation is based on transitions between scattering states and contacts. The first problem we have to handle is to find the scattering states. Standing wave decomposition is our choice. First, we consider the open system as closed by solving the one dimension time independent schrödinger equation

$$-\frac{\hbar^2}{2}\frac{d}{dx}(\frac{1}{m^*}\frac{d\Psi_p(x)}{dx}) + V(x)\Psi_p(x) = E_p\Psi(x), \tag{3.1}$$

twice with two different boundary conditions to obtain enough standing wave states. The two different boundary conditions are Dirichlet boundary condition and Neumann boundary conditions:

$$\begin{cases} \Psi_p|_{x=0,\ L} = 0,\ Dirichlet \\ \dfrac{d\Psi_p}{dx}|_{x=0,\ L} = 0,\ Neumann \end{cases} \tag{3.2}$$

Dirichlet boundary condition requires the wave function to be zero at boundaries and the Neumann boundary condition requires the derivative of wave function to be zero at boundaries. They are also known as sine-like and cosine-like solutions. The reason is following. Since there is no current in a close system, wave function must only contain the real part, we can write the analytical solution in a general form

$$\Psi_p(x) = A_p sin(kx + \theta), \tag{3.3}$$

with its derivative

$$\frac{d\Psi_p(x)}{dx} = A_p kcos(kx + \theta), \tag{3.4}$$

where A_p is the amplitude and $\theta \in (-\frac{\pi}{2}, \frac{\pi}{2}]$ is the phase shift. For the Dirichlet boundary condition $\Psi_p(x)|_{x=0,\ L} = 0$, we have $\theta = 0$, yielding $\Psi_p(x) = A_p sin(kx)$, which is sine-like. For the neumann boundary condition, $\frac{d\Psi_p(x)}{dx}|_{x=0,\ L} = 0$, we have $\theta = \frac{\pi}{2}$, yielding $\Psi_p(x) = A_p cos(kx)$ which is cosine-like. Our discretization of the continuous energy spectrum is complete and robust. Fig. 3.2 shows the occupation of states after self-consistency obtained in a 1D *n-i-n* device at equilibrium. Solid rectangles are the original data which does not fit the usual distribution of density versus energy based on the Fermi-Dirac function. But if we apply Fast Fourier transform (FFT), the average effect (shown as a solid red line) is exactly the desired distribution. Therefore our approach is mathematically correct to illustrate the system and the physics meaning can be interpreted if we consider the net effect.

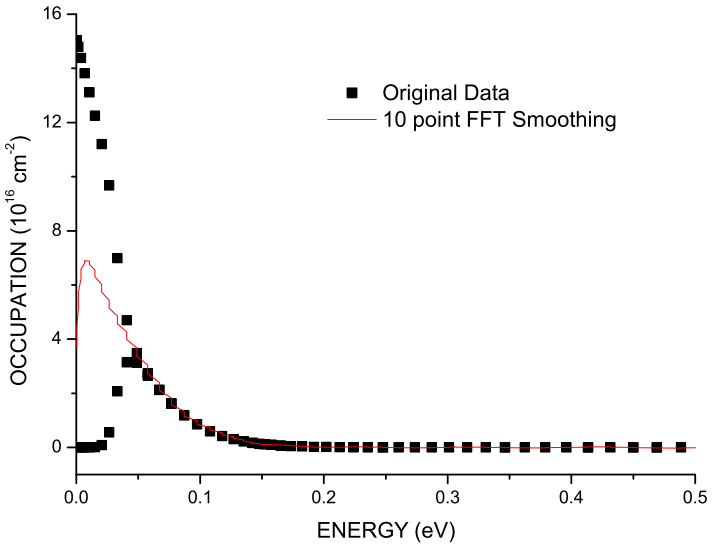

Figure 3.2. 1D *n-i-n* device electron occupation of states at equilibrium (black rectangular dots) and its FFT average (red solid line).

Mathematically, mixed boundary conditions other than sine and cosine are not necessary. The reason is that sine-like and cosine-like solutions are the orthogonal basis of the whole solution space; any other solution could be expressed as a linear

combination of them. It can not offer more accurate result. On the contrary one has to solve non-linear eigenvalue problems, because sine-like and cosine-like are the only linear cases. Normalization will be another problem for mixed boundary conditions. Sine and cosine are orthogonal and each carries a weight of 1, when both of them are included we can simply normalized to $\frac{1}{2}$. Other phases rather than 0 and $\frac{\pi}{2}$ need to find its own weight first. That's the reason why the inclusion of $\pm\frac{\pi}{4}$ with the normalization of $\frac{1}{4}$ does not work properly[17].

After two sets standing wave solutions $\{E_p^{sin},\Psi_p^{sin}\}$ and $\{E_p^{cos},\Psi_p^{cos}\}$ are obtained, the eigen values and eigen functions containing enough information to represent the local density of states of the device, we need to decompose standing waves into traveling waves injected from two contacts. For a given injecting energy E_p, traveling waves at the boundary i can be written as

$$\Phi_p^i(x) = a_p^i e^{-ik_p^i x} + b_p^i e^{ik_p^i x}, \tag{3.5}$$

where $a_p^i e^{-ik_p^i x}$ is the incoming wave with a_p^i its injection amplitude and $b_p^i e^{ik_p^i x}$ is the reflection wave with b_p^i the reflection amplitude as shown in Fig. 3.3.

Decomposing Eq. (3.3) in the same form as Eq. (3.5)

$$\Psi_p(x) = \frac{iA_p}{2} e^{-i\theta} e^{-ik_p x} + \frac{A_p}{2i} e^{i\theta} e^{ik_p x}, \tag{3.6}$$

we can easily have the injection amplitude

$$a_p^i = \frac{iA_p^i}{2} e^{-i\theta}. \tag{3.7}$$

Finding the value of A_p^i is even straight forward. For $\theta = 0$, sine-like, $\Psi_p(x)|_{x=0,\ L} = 0$, from Eq. (3.4),

$$A_p^i = \frac{1}{k_p^i cos\theta} \frac{d\Psi_p(x)}{dx}|_{x=0,\ L} = \frac{1}{k_p^i} \frac{d\Psi_p(x)}{dx}|_{x=0,\ L}. \tag{3.8}$$

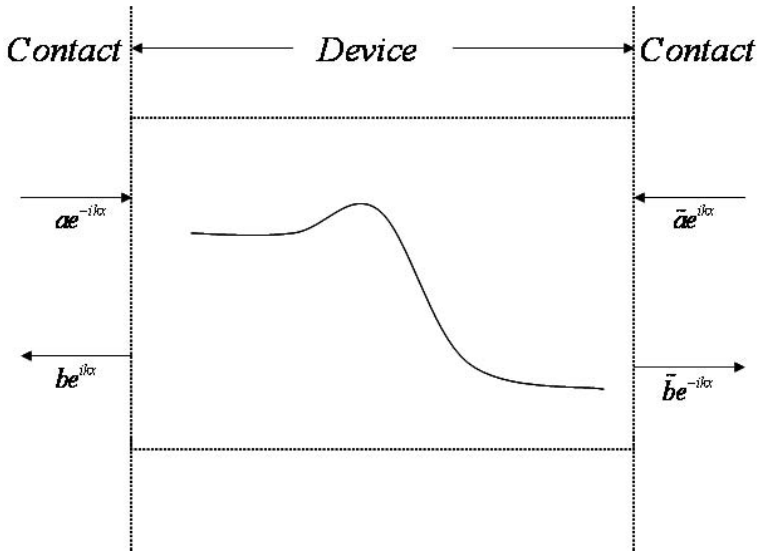

Figure 3.3. Incoming wave ae^{-ikx} with its reflection wave be^{ikx} from left; incoming wave $\tilde{a}e^{ikx}$ with its reflection wave $\tilde{b}e^{-ikx}$ from right.

Similarly, for $\theta = \frac{\pi}{2}$, cosine-like, $\frac{d\Psi_p(x)}{dx}|_{x=0,\ L} = 0$, from Eq. (3.3),

$$A_p^i = \frac{1}{sin\theta}\Psi_p(x)|_{x=0,\ L} = \Psi_p(x)|_{x=0,\ L}. \tag{3.9}$$

There is an interesting phenomenon that regardless of the injection energy is of sine-like or cosine-like, its amplitude only depends on the standing wave solution at the contact. For sine-like it depends on the derivative of standing wave, while for cosine-like it depends on the standing wave itself. In another word, what happens inside the device has no direct influence on the injection amplitude. This result still stands in the two dimension case as will be show in the next section.

We have solved the closed system and obtained the injection energy along with their amplitude for traveling waves from both contacts. E_p^{sin} and E_p^{cos} are then together arranged from low to high and truncated at a point E_{max} (typically $E_{max} = E_F^{high} + 20k_BT$) where the occupation is insignificant to reduce the computation cost . The next step consists calculating all the traveling states by solving the open boundary condictions Shrödinger equation which can be written as:

$$[E_p I - H - \Sigma_1 - \Sigma_2]\Phi_p^i = S_p^i = i\gamma_p^i, \tag{3.10}$$

where H is the system Hamiltonian, E_p is the injection energy, I is identity matrix, Σ_1 and Σ_2 are the self-energy terms describing the interaction with two contacts, right hand side of the equation is known as the source term (S_p^i) and the broadening effect ($i\gamma_p^i$). Eq. (3.10) is given in a matrix form similar to the NEGF approach. Instead of inverting the left hand side to obtain the retarded Green's function, we simply solve this linear equation to find the traveling states Φ_p^i.

Since the eigenstates are doubly sampled and each set has a weight of 1, for a given energy E_p^i injected from contact i the traveling wave function must be normalized as

$$\int_0^L (\sum_{i=1}^{2} |\Phi_p^i(x)|^2) = \frac{1}{2}, \tag{3.11}$$

where $\Phi_p^i(x)$ is the traveling wave injected from contact i (cathode to the anode or anode to the cathode in 1D). The occupation of the individual state p of contact i is given by

$$\rho_p^i = \int_0^\infty dE_\perp \cdot 2 \cdot \frac{1}{2\pi} \frac{dk_T}{dE_\perp} f_{FD}(E_F^i, E_\perp, E_p^i), \tag{3.12}$$

where

$$f_{FD}(E_F^i, E_\perp, E_p^i) = \frac{1}{1 + e^{\frac{E_p^i + E_\perp - E_F^i}{k_B T}}} \tag{3.13}$$

is the Fermi-Dirac distribution. $E_\perp$ is the kinetic energy corresponding to motion in the infinite transverse plane not included in the simulation domain. E_F^i is the Fermi level at contact i which has to be adjusted to satisfy charge neutrality at the boundaries before the Schrödigner-Poisson loop starts because the discretization of the continuous energy changes its value. Inserting Eq. (3.13) into Eq. (3.12) and integrating, ρ_p^i has a simple explicit expression in 1D

$$\rho_p^i = \frac{m^* k_B T}{\pi \hbar^2} ln(1 + e^{\frac{E_F^i - E_p^i}{k_B T}}). \tag{3.14}$$

The electron density therefore can be written as:

$$n(x) = \sum_{i=1}^{2} \sum_{p=1}^{max} \rho_p^i |\Phi_p^i(x)|^2. \tag{3.15}$$

When a self-consistent solution is sought, one can find that charge neutrality at boundaries is hard to achieve especially under high bias voltage, due to the open nature of the device. When bias is applied, electrons move from cathode to the anode creating current. As a whole system, electrons flowing from cathode to anode will eventually come back to the cathode via the external circuit, but this external circuit is not included in our simulation domain. So the net effect is that charge is missing at the source and gathering at the drain as shown in Fig. 3.4(a).

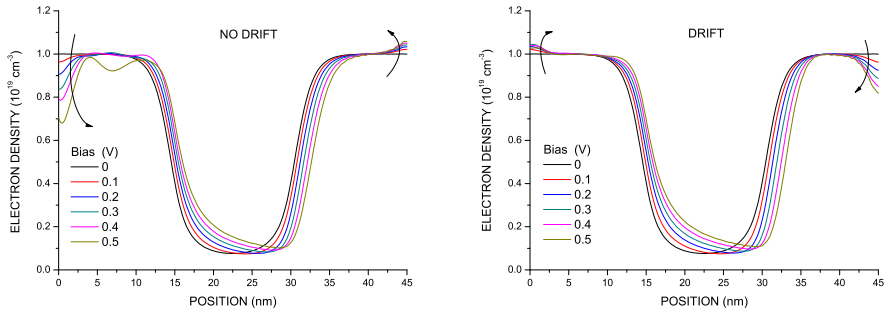

(a) (b)

Figure 3.4. 1D *n-i-n* (each region being 15nm, n being $10^{19} cm^{-3}$) self-consistent electron density under various bias (a) without and (b) with drift wave vector. Arrow direction shows the increase of bias voltage.

The use of periodic boundary condition may help to solve this problem, but it changes the system to be quasi-open, and it cannot include far-from-equilibrium which is of interest because periodic boundary conditions are enforceable only at equilibrium. This problem affects all quantum transport simulations, but it may not be obvious in the literature because of following reasons [22, 9]: (1) devices operating near equilibrium are minimally affected; (2) floating boundary conditions are used to

solve Poisson equation, thus forcing the potential to be "flat" near the contacts; (3) the Fermi level is not as the same as at the contact but adjusted in a self-consistent way; (4) very high doping is used to minimize the potential change; (5) a drift wave vector k_D is introduced. Since there is no perfect model for the contact, every method mentioned above has its own merit in a certain sense. Because of the clear physics meaning, we favor the k_D drift vector approach. Its improved result is compared in Fig. 3.4(b).

Eq. (3.14) shows that occupation relies on the Fermi energy of the contact. When the device is operating under non-equilibrium, a feedback drift wave vector from device to the contact will change the Fermi-Dirac distribution in Eq. (3.13) and eventually occupy traveling states "correctly" to satisfy charge neutrality. Suppose the drift wave vector in the transport direction is k_D, then the total energy can be written as

$$E = \frac{\hbar^2(k-k_D)^2}{2m^*} + E_\perp = \frac{\hbar^2 k^2}{2m^*} + \frac{\hbar^2 k_D(k_D-2k)}{2m^*} + E_\perp, \tag{3.16}$$

substitute $\frac{\hbar^2 k^2}{2m^*} = E_p$ we have

$$E = E_p + \frac{\hbar^2 k_D(k_D-2k)}{2m^*} + E_\perp. \tag{3.17}$$

It is obvious that the longitudinal energy is shifted from E_p to $E_p + \frac{\hbar^2 k_D(k_D-2k)}{2m^*}$ due to the drift vector. Updating E_p^i in Eq. (3.13), a new expression for the drifted Fermi-Dirac distribution is obtained as:

$$f_{FD}(E_F^i, E_\perp, E_p^i) = \frac{1}{1+e^{\frac{E_p^i + \frac{\hbar^2 k_D^i(k_D^i-2k_p^i)}{2m^*} + E_\perp - E_F^i}{k_B T}}}, \tag{3.18}$$

and updating E_p^i in Eq. (3.14), the drifted occupation of each state becomes:

$$\rho_p^i = \frac{m^* k_B T}{\pi \hbar^2} ln(1 + e^{\frac{E_F^i - E_p^i - \frac{\hbar^2 k_D^i (k_D^i - 2k_p^i)}{2m^*}}{k_B T}}). \tag{3.19}$$

The determination of k_D can be done in several ways. It can be directly set by satisfying charge neutrality at the contact, or conserving current flux in the device and contact, or even some higher moment (such as energy) continuity at boundaries. Enforcing continuity of higher moments of the distribution is a hard numerical task. We have tried the other two and find charge neutrality works but not as well as current flux conservation. So k_D^i is chosen to satisfy current continuity equation $J_{dev}^i = J_{cont}^i$.

The current density in the device can be expressed as

$$J_{dev}^i = -\frac{ie\hbar}{2m^*} \sum_{i=1}^{2} \sum_{p=1}^{max} \rho_p^i \cdot 2Im[(\nabla \Phi_p^i)^* \Phi_p^i] \cdot (-\hat{n}), \tag{3.20}$$

and the current density at the contact i is given

$$J_{cont}^i = -e\frac{\hbar k_D^i}{m^*} n^i, \tag{3.21}$$

where n^i is the electron density at the interface of device and contact.

After including k_D we can obtain the correct occupation and electron density. Thus we can solve Poisson equation:

$$-\nabla(\varepsilon(x)\nabla\varphi(x)) = e(N_D(x) - n(x)). \tag{3.22}$$

The solution φ is then back to $E_c = \Delta E_c - e\varphi$ where ΔE_c is the conduction band offset by different materials. When coupled to the Schrödinger equation, Poisson equation is nonlinear. Newton-Raphson method [3] is usually needed to improve convergence. But unlike traditional coupled Schrödinger-Poisson solvers, the introduction of drift wave vector makes the formulation slightly different.

Using the FEM method to discretize Eq. (3.22), we have:

$$T_{P_{n\times n}}\varphi_{n\times 1} = D_{n\times n}(N_d - n)_{n\times 1}, \tag{3.23}$$

T_P is the mass matrix and D is the stiffness matrix. They both capture the operator $-\frac{\nabla(\varepsilon(x)\nabla)}{e}$. Define $f_{P_{n\times 1}} := T_{P_{n\times n}}\varphi_{n\times 1} - D_{n\times n}(N_d - n)_{n\times 1}$.

Similarly the current continuity equations can be written in a matrix form as:

$$J_{dev_{2\times 1}} = J_{cont_{2\times 1}}. \tag{3.24}$$

The matrix has 2 rows because there are two contacts in the 1D case. Define $f_{J_{2\times 1}} := J_{dev_{2\times 1}} - J_{cont_{2\times 1}}$.

The total unknowns we need to find are vectors $\varphi_{n\times 1}$ and $k_{D_{2\times 1}}$. Put Eq. (3.23) and Eq. (3.24) into a big matrix, and define

$$f_{(n+2)\times 1} := \begin{pmatrix} f_{P_{n\times 1}} \\ f_{J_{2\times 1}} \end{pmatrix}, \tag{3.25}$$

correspondingly the unknowns can be written

$$x_{(n+2)\times 1} := \begin{pmatrix} \varphi_{n\times 1} \\ k_{D_{2\times 1}} \end{pmatrix}. \tag{3.26}$$

Now it is very clear that we need to find $x_{(n+2)\times 1}$ such that $f_{(n+2)\times 1} = 0$. After this simple transform, we can now apply the standard Newton method. Its Jacobian matrix is calculated by

$$\frac{df}{dx} = \begin{pmatrix} \frac{\partial f_P}{\partial \varphi} & \frac{\partial f_P}{\partial k_D} \\ \frac{\partial f_J}{\partial \varphi} & \frac{\partial f_J}{\partial k_D} \end{pmatrix}. \tag{3.27}$$

The term $\frac{\partial f_P}{\partial \varphi}$ measures how electron density changes as the potential changes. Apply the definition of f_P, we have $\frac{\partial f_P}{\partial \varphi} = \frac{\partial(T_{P_{n\times n}}\varphi_{n\times 1} - D_{n\times n}(N_d - n)_{n\times 1})}{\partial \varphi_{n\times 1}} = T_{P_{n\times n}} +$

$D_{n\times n}(\frac{\partial n_{n\times 1}}{\partial \varphi_{n\times 1}})_{n\times n}$. The physics meaning becomes clearer. But it is not easy to calculate the correct value simply because local density does not only depend on the local potential. Any feedback of local potential will influence on the global density by solving the Schrödinger equation. We can evaluate it using semiclassical approximation that $\frac{\partial n}{\partial \varphi} = \frac{e}{k_B T} N_c \frac{2}{\sqrt{\pi}} \frac{1}{2} F_{-\frac{1}{2}}(\frac{E_F^{local} - \Delta E_c + e\varphi}{k_B T})$, where E_F^{local} is the local fermi level. It has been tested that even the non-degenerate approximation $\frac{\partial n}{\partial \varphi} = n\frac{e}{k_B T}$ ("mistakenly" estimate $F_{-\frac{1}{2}}$ with $F_{\frac{1}{2}}$) can give good convergence result. This treatment comes from random phase approximation (RPA), which can be proven by using time independent perturbation [25].

The term $\frac{\partial f_P}{\partial k_D}$ is the influnce of drift vector (current) on the electron density in the device. Since we have the analytical expression in Eq. (3.15) and Eq. (3.19), although tedious its explanation is straightforward.

$\frac{\partial f_J}{\partial \varphi}$ describes the current density behavior as the potential changes. The current density in the device is calculated by Eq. (3.20). It depends on the occupation of states ρ_p^i and the flux term $Im[(\nabla \Phi_p^i)^* \Phi_p^i]$. A sudden perturbation of potential will affect both terms via the solution of Schrödinger equation, but unfortunately there is no easy way to evaluate this change. Numerical evaluation by the secant method does not give good results, as discovered by Laux [17]. In that paper this value is set to zero (imply no connection) and we follow the same procedure. The non-quadratic convergence characteristics and soft-convergence may be related to this choice. We leave the open question for now.

The term $\frac{\partial f_J}{\partial k_D}$ expresses the relation between current and drift vector. This can be analytically done from Eq. (3.20) and Eq. (3.21).

Linearizing Eq. (3.25), we have:

$$x_{j+1} = x_j - (\frac{df}{dx_j})^{-1} f(x_j). \tag{3.28}$$

Starting from some initial guess x_0 (for $\varphi_{n\times n}$ we can use the self-consistent semi-classical solution, $k_{D_{2\times 1}}$ can be set to zero or to the value the bias point calculated previously), coupled with Schrödinger Eq. (3.10) we continue the iteration of Eq. (3.28) under the proper boundary conditions to calculate x_j (j=1,2,3 ...), until a required convergence criteria is met, leading to the ballistic solution.

3.1.2 Scattering

In order to solve the PME by the MC method in the similar framework as BTE, classical representative electrons have to be assigned to each state according to their occupation. Assume a total number N_{tot} of super-particles, the weight carried by each "electron" will be

$$\omega = \frac{\int_0^L dx n(x)}{N_{tot}} \tag{3.29}$$

in units of m^{-2}. Applying this to Eq. (3.19), the occupation of each state p associate with contact i can be represented by electrons with number $N_p^i = \rho_p^i/\omega$. For an electron j ($j \leq N_p^i$) in such state, its total energy is $E_p^{ij} = E_p^i + E_{p_\perp}^{ij}$. Note that electrons occupying the same state have the same longitudinal energy E_p^i. The scattering rate depends on the total energy, so a transverse energy $E_{p_\perp}^{ij}$ must be assigned to each electron individually based on the product of density of state and the Fermi-Dirac distribution in Eq. (3.18). Thanks to the simple 2D density of state ($m^*/\pi\hbar^2$ in 1D transport, independent of energy), this can be done analytically following the direct technique [11]:

$$E_{p_\perp}^{ij} = E_F^i - E_p^i - \frac{\hbar^2 k_D^i (k_D^i - 2k_p^i)}{2m^*} - k_B T\{ln[(1 + e^{\frac{E_F^i - E_p^i - \frac{\hbar^2 k_D^i (k_D^i - 2k_p^i)}{2m^*}}{k_B T}})^r - 1]\} \tag{3.30}$$

where $r \in (0, 1)$ is a pseudo-random number. On the other hand in 2D or 3D transport simulations, since the integral over energy cannot be done analytically, a conventional rejection technique [11] has to be used. This usually requires additional CPU time as will be shown in the next section.

The Master equation for an open system can be written as:

$$\frac{\partial \rho_u}{\partial t} = \sum_v (W_{uv}\rho_v - W_{vu}\rho_u) + [\frac{\partial (f_u - \rho_u)}{\partial t}]_{res}, \tag{3.31}$$

where $u, v \in p$. Applying the Fermi golden rule, the transition rate W_{uv} from v to u can be evaluated as:

$$W_{uv} = \frac{2\pi}{\hbar} | < u|H_{int}|v > |^2 \delta(E_u - E_v \pm \hbar\omega_q), \tag{3.32}$$

where H_{int} is the interaction Hamiltonian, δ function conserves the energy, E_u and E_v are the total energy for electrons in states u and v respectively, ω_q is the phonon frequency or zero if the scattering process is elastic. Note in 3.32 the extra term the form factor $F_{vi'ui}$, distinguishing the result from semi-classical particles:

$$F_{vi'ui} = \int_0^L dx |\Phi_v^{i'}(x)|^2 |\Phi_u^i(x)|^2. \tag{3.33}$$

Calculation of form factor can be very time consuming due to the large amount of scattering states and to the numerical calculation of the integral itself. We store it in a look-up table and update it when at each Schrödinger-Poisson update.

Having fixed a small time δt ($\approx 10^{-15}s$), for an electron j in state u occupied by the injection from contact i, the scattering probability will be:

$$P_u^{ij} = \delta t \sum_v W_{uv} = \frac{\delta t}{\tau_u^{ij}} \tag{3.34}$$

Similarly to the Monte Calor in the semi-classical case, the probability for all scattering processes can be calculated and compared to a random number to select the process occurring at a given time step. Figure 3.5 demonstrates how the selection process works.

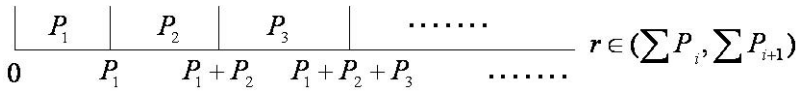

Figure 3.5. Scattering process P_{i+1} happens when random number r falls into the interval $(\sum P_i, \sum P_{i+1})$.

We loop over all contacts and scattering states to finish the scattering processes in the device. Then the phenomenological treatment of the contact starts. For a state u populated by contact i, the electron occupation in the device ρ_u^i is compared with the population f_u^i. If $\rho_u^i > f_u^i$, then the net electron flux $(\frac{f_u^i - \rho_u^i}{\omega})$ will be injected into the device at a rate $\frac{\hbar k_u^i}{m^*}|A_u^i|^2$, and vice-versa.

The number of super-particles can be converted to electron density after completion of scattering processes and exchange with contacts. The Poisson equation is solved again and the new potential is used to solved the Schrödinger equation, thus obtaining new scattering states. The new potential is treated as a sudden perturbation and super-particles are assigned to these new states with the probability based on the overlap factor between the old state $|ui>$ and the new state $< u'i|$

$$F_{ui,u'i} = | < u'i|ui > |^2. \tag{3.35}$$

Similar to the procedure of simulating the scattering processes, rejection technique is applied. The only difference is that the reassignment of electrons is among the states from the same contact because the electron transport direction is conserved.

The iteration of Monte Carlo, Poisson and Schrödinger continues until the potential, the occupation of states and the current do not show any significant change. Due to the random noise induced by Monte Carlo, we are not expecting to achieve the same accuracy as in the ballistic case. Figure 3.6 shows the current behavior in a iteration process of 2D Taper device at $V_{DS} = 0.3V$, V_{GS} varies from 0 to 0.3V.

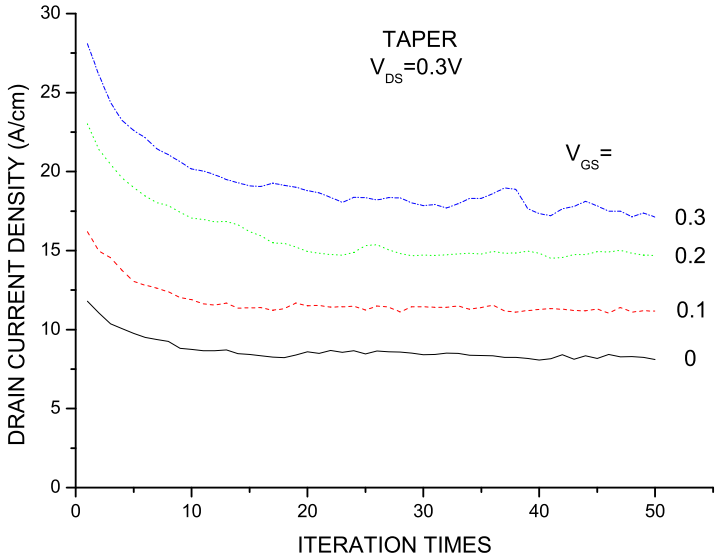

Figure 3.6. Current behavior in a iteration process of 2D Taper device at $V_{DS} = 0.3V$, V_{GS} varies from 0 to 0.3V.

3.2 PME in 2D

2D open system can be partitioned into device region Ω_0, lead regions Ω_i(i=1,2,3...) as shown in Fig. 3.7. The boundary that Ω_i and Ω_0 meet is Γ_i, other boundaries are Γ_0.

3.2.1 Ballistic solution

Unlike in 1D, charge neutrality at the contact is no longer at certain point, in 2D it is the integral along the Γ_i. First we need to find the 1D Schröndinger-Poisson self-consistent solution for all the Γ_i [18] and use the obtained potential as the fixed boundary condition in the following 2D simulation. Define a local coordinate (η_i,ξ_i) at the contact Γ_i as shown in Fig. 3.8. The Schröndinger equation therefore can be written as:

$$-\frac{\hbar^2}{2}[\frac{d}{d\xi_i}(\frac{1}{m^*_{\xi_i}(\xi_i)}\frac{d\chi^i_m(\xi_i)}{d\xi_i})] + V(\xi_i)\chi^i_m(\xi_i) = E^i_m\chi^i_m(\xi_i), \tag{3.36}$$

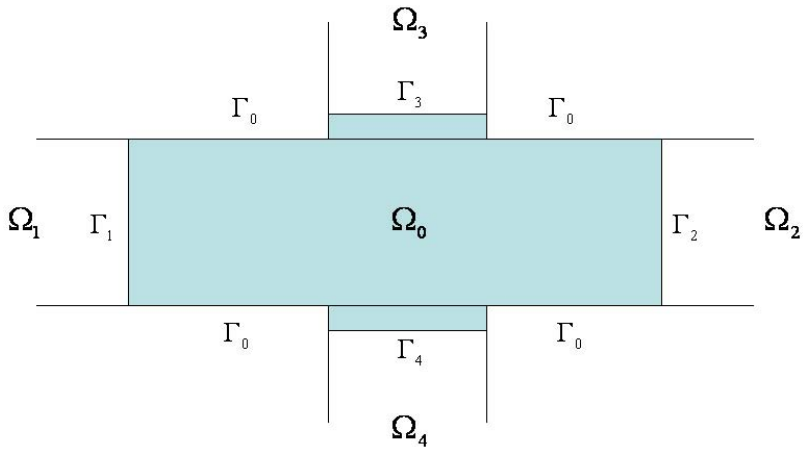

Figure 3.7. Partition of 2D geometry. Ω_0 is the device region; Ω_i (i=1,2,3...) is the lead region and Γ_i is the boundary where they meet. Other boundary of Ω_0 is Γ_0.

with the boundary condition $\chi^i_m(0) = \chi^i_m(d_i)$, where m stands for different modes, $m^*_{\xi_i}(\xi_i)$ is the effective mass, allowed to be space dependent. $\chi^i_m(\xi_i)$ is the wave function of m^{th} mode at contact i. Being the orthogonal basis, it needs to be normalized as

$$\int_0^{d_i} \chi^i_l(\xi_i)\chi^i_m(\xi_i)d\xi_i = \delta_{lm}. \tag{3.37}$$

Similar to Eq. (3.14) and Eq. (3.15), the electron density along the lead is

$$n(\xi_i) = \sum_m \frac{m^*_{\xi_i} k_B T}{\pi\hbar^2} ln(1 + e^{\frac{E^i_F - E^i_m}{k_B T}})|\chi^i_m(\xi_i)|^2. \tag{3.38}$$

The poisson equation

$$-\nabla(\varepsilon(\xi_i)\nabla\varphi(\xi_i)) = e(N_D(\xi_i) - n(\xi_i)) \tag{3.39}$$

is then solved with neumann boundary condition $\frac{\partial\varphi}{\partial\xi_i}|_{\xi_i=0} = \frac{\partial\varphi}{\partial\xi_i}|_{\xi_i=d_i} = 0$. Once self-consistency is achieved, the line integral of charge ($\int_o^{d_i} d\xi_i(n(\xi_i) - N_D(\xi_i))$) should be compared with zero to check whether charge neutrality is satisfied. If not, change the initial guess of the mid-point potential and continue the iteration. Standard secant

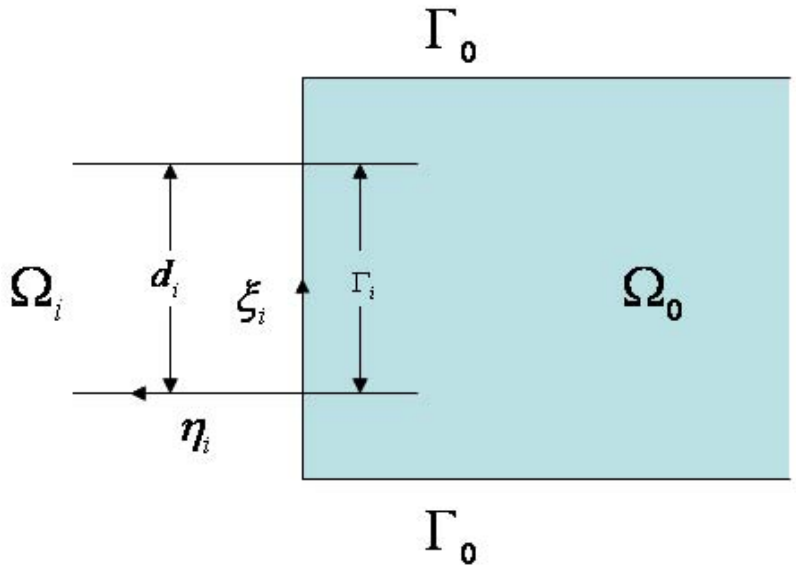

Figure 3.8. Local coordinate (η_i,ξ_i) at contact Γ_i where η_i is along the transport direction. d_i is the lead width of Ω_i.

method [3] can be applied to make it converge fast. Figure 3.9 shows the converged simulation result of a 3nm and 6nm boundary respectively.

Solving the 2D problem semi-classically with the Thomas-Fermi approximation, gives an initial guess of the potential which can be smoothed by solving 2D Poisson equation again applying the converged electron density but use $\varphi(\xi_i)$ as boundary conditions. Use the smoothed potential to solve 2D Schrödinger equation

$$-\frac{\hbar^2}{2}[\frac{\partial}{\partial x}(\frac{1}{m^*}\frac{\partial \Psi_p(x,y)}{\partial x}) + \frac{\partial}{\partial y}(\frac{1}{m^*}\frac{\partial \Psi_p(x,y)}{\partial y})] + V(x,y)\Psi_p(x,y) = E_p\Psi_p(x,y) \quad (3.40)$$

with dirichlet and neumann boundary conditions. The general solution at contact i is

$$\begin{aligned}\Psi_p(\eta_i,\xi_i) = &\sum_{m=1}^{N_p^i} A_{pm}^i \chi_m^i(\xi_i) sin(k_{pm}^i \eta_i + \theta_i) \\ &+ \sum_{m=N_p^i+1}^{M^i-2} \frac{A_{pm}^i}{2} \chi_m^i(\xi_i)[e^{-ik_{pm}\eta_i} - cot(\theta_i + \frac{\pi}{4})e^{ik_{pm}\eta_i}],\end{aligned} \quad (3.41)$$

with its derivative

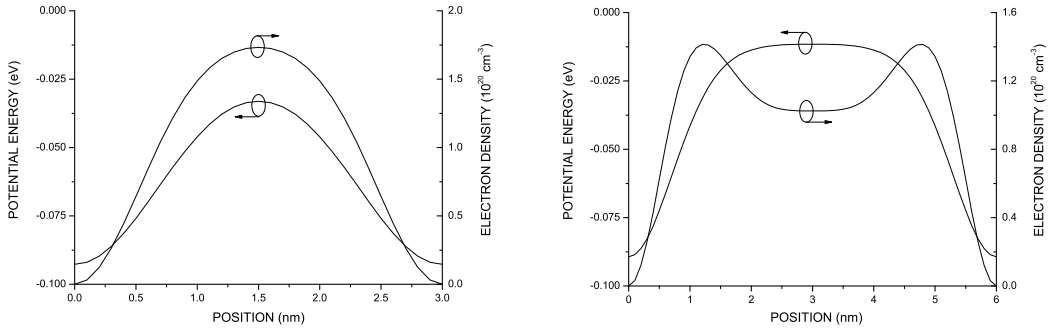

(a) (b)

Figure 3.9. Electron density and potential energy of 1D self-consistent solution of (a) 3nm and (b) 6nm boundary.

$$\begin{aligned}\frac{\partial \Psi_p(\eta_i,\xi_i)}{\partial \eta_i} &= \sum_{m=1}^{N_p^i} A_{pm}^i k_{pm}^i \chi_m^i(\xi_i) cos(k_{pm}^i \eta_i + \theta_i) \\ &- \sum_{m=N_p^i+1}^{M^i-2} \frac{iA_{pm}^i}{2} k_{pm}^i \chi_m^i(\xi_i)[e^{-ik_{pm}\eta_i} + cot(\theta_i + \frac{\pi}{4}) e^{ik_{pm}\eta_i}],\end{aligned} \tag{3.42}$$

where A_{pm}^i is the amplitude of the m^{th} mode of energy state p, and k_{pm}^i is the corresponding wave vector. Note k_{pm}^i is real when $1 \leq m \leq N_p^i$ ($E_p > E_m^i$) and is imaginary when $m \geq N_p^i + 1$ ($E_p < E_m^i$). The summation is ideally to be infinity but it is constrained by the numerical implementation. Since E_m^i is obtained from the Eq. (3.36), the maximum m is the number of boundary nodes M^i minus 2.

Follow the same procedure in 1D when $\theta_i = 0$ we can derive that sine-like solution

$$\Psi_p(\eta_i,\xi_i) = \sum_{m=1}^{N^i} A_{pm}^i \chi_m^i(\xi_i) sin(k_{pm}^i \eta_i) - i \sum_{m=N^i+1}^{M^i-2} A_{pm}^i \chi_m^i(\xi_i) sin(k_{pm}^i \eta_i), \tag{3.43}$$

and cosine-like solution when $\theta_i = \frac{\pi}{2}$

$$\Psi_p(\eta_i,\xi_i) = \sum_{m=1}^{M_i-2} A_{pm}^i \chi_m^i(\xi_i) cos(k_{pm}^i \eta_i). \tag{3.44}$$

As mentioned, in 2D because of the existence of evanescent waves, the boundary condition formation is more complicated than 1D. We apply the quantum transmitting boundary method (QTBM) proposed by Lent and Kirkner [19] and developed by Laux [17]. Traveling waves in lead i can be written as

$$\Phi_p^i(\eta_i,\xi_i) = \sum_{m=1}^{M^i-2} [a_{pm}^i \chi_m^i(\xi_i) e^{-ik_{pm}^i \eta_i} + b_{pm}^i \chi_m^i(\xi_i) e^{ik_{pm}^i \eta_i}] \tag{3.45}$$

where a_{pm}^i is the injection amplitude of the m^{th} mode, and b_{pm}^i is the corresponding refection amplitude. $\chi_m^i(\xi_i)$ is the 1D wave function of the m^{th} mode distinguishing the expression in Eq. (3.5). Note in Laux paper he claims that $a_{pm}^i \neq 0$ when $m \geq N^i + 1$ which is different from Lent and Kirkner's formulation. We followed his method. They both separate Eq. (3.45) into a real wave vector part and an imaginary wave vector part, but indeed the expression is the same for both cases. Here, we choose to write it in this concise way.

Decompose Eq. (3.41) into the same format as Eq. (3.45)

$$\begin{aligned}\Psi_p(\eta_i,\xi_i) =& \sum_{m=1}^{N_p^i} \frac{iA_{pm}^i}{2} \chi_m^i(\xi_i) e^{-ik_{pm}\eta_i} e^{-i\theta} + \sum_{m=1}^{N_p^i} \frac{A_{pm}^i}{2i} \chi_m^i(\xi_i) e^{ik_{pm}\eta_i} e^{i\theta} \\ &+ \sum_{m=N_p^i+1}^{M^i-2} \frac{A_{pm}^i}{2} \chi_m^i(\xi_i) e^{-ik_{pm}\eta_i} - \sum_{m=N_p^i+1}^{M^i-2} \frac{A_{pm}^i}{2} \chi_m^i(\xi_i) cot(\theta_i + \frac{\pi}{4}) e^{ik_{pm}\eta_i}],\end{aligned} \tag{3.46}$$

compare, we have

$$\begin{aligned} a_{pm}^i =& \frac{iA_{pm}^i}{2} e^{-i\theta}, \ \ 1 \leq m \leq N_p^i \\ =& \frac{A_{pm}^i}{2}, \quad m \geq N_p^i + 1 \end{aligned} \tag{3.47}$$

For $\theta = 0$, sine-like, $\Psi|_{\Gamma_i} = 0$, Eq. (3.42) simplifies to

$$\frac{\partial \Psi_p(\eta_i,\xi_i)}{\partial \eta_i}|_{\eta_i=0} = \sum_{m=1}^{N_p^i} A_{pm}^i k_{pm}^i \chi_m^i(\xi_i) - i \sum_{m=N_p^i+1}^{M^i-2} A_{pm}^i k_{pm}^i \chi_m^i(\xi_i), \tag{3.48}$$

therefore,

$$\begin{aligned} A^i_{pm} =& \frac{1}{k^i_{pm}} \int_0^{d_i} \chi^i_m(\xi_i) \frac{\partial \Psi_p(\eta_i, \xi_i)}{\partial \eta_i}|_{\eta_i=0} d\xi_i, \;\; 1 \le m \le N^i_p \\ =& \frac{i}{k^i_{pm}} \int_0^{d_i} \chi^i_m(\xi_i) \frac{\partial \Psi_p(\eta_i, \xi_i)}{\partial \eta_i}|_{\eta_i=0} d\xi_i, \quad m \ge N^i_p + 1 \end{aligned} \tag{3.49}$$

substitute back into Eq. (3.47), we can reach an elegant expression similar to 1D case for all $1 \le m \le M^i - 2$

$$a^i_{pm} = \frac{i}{2k^i_{pm}} \int_0^{d_i} \chi^i_m(\xi_i) \frac{\partial \Psi_p(\eta_i, \xi_i)}{\partial \eta_i}|_{\eta_i=0} d\xi_i. \tag{3.50}$$

For $\theta = \frac{\pi}{2}$, cosine-like, $\frac{\partial \Psi}{\partial \eta}|_{\Gamma_i} = 0$, Eq. (3.41) simplifies to

$$\Psi_p(\eta_i, \xi_i) = \sum_{m=1}^{M^i-2} A^i_{pm} \chi^i_m(\xi_i), \tag{3.51}$$

therefore, for $1 \le m \le M^i - 2$

$$A^i_{pm} = \int_0^{d_i} \chi^i_m(\xi_i) \Psi_p(\eta_i, \xi_i)|_{\eta_i=0} d\xi_i, \tag{3.52}$$

hence,

$$a^i_{pm} = \frac{1}{2} \int_0^{d_i} \chi^i_m(\xi_i) \Psi_p(\eta_i, \xi_i)|_{\eta_i=0} d\xi_i. \tag{3.53}$$

Arrange standing wave states according to the energy increases, the schrödinger equation is ready to be solved:

$$[E_p I - H - \sum_i^n] \Phi^i_p = S^i_p = i\gamma^i_p, \tag{3.54}$$

where $\sum_i^n$ sums all of contacts. Follow the same procedure in 1D to normalize wave functions and then electron occupation in 2D is given by:

$$\rho^i_p = \frac{\sqrt{2m^* k_B T}}{\pi \hbar} F_{-\frac{1}{2}}\left(\frac{E^i_F - E^i_p - \frac{\hbar^2 k^i_D (k^i_D - 2k^i_p)}{2m^*}}{k_B T}\right), \tag{3.55}$$

if drift wave vector k_D is taken into consideration. $F_j(x) = \int_0^\infty dt \frac{t^j}{e^{t-x}+1}$ is the complete Fermi-Dirac integral to the order of j. In this notation, $F_j(x) = \mathcal{F}_j(x)\Gamma(j+1)$. Since $\frac{d\mathcal{F}_j(x)}{dx} = \mathcal{F}_{j-1}(x)$, we have $\frac{dF_j(x)}{dx} = \Gamma(j+1)\mathcal{F}_{j-1}$, which is helpful to evaluate the Jacobian matrix. The electron density then is

$$n(x,y) = \sum_{i=1}^{n} \sum_{p=1}^{max} (\sum_{m=1}^{M^i-2} c_{pm}^i \rho_p^i) |\Phi_p^i(x,y)|^2, \tag{3.56}$$

where c_{pm}^i is the weighting factor for injection energy E_p from contact i, weighted at transverse energy level E_m^i. It can be obtained from a_{pm}^i

$$c_{pm}^i = |a_{pm}^i|^2 / \sum_{m=1}^{M^i-2} |a_{pm}^i|^2. \tag{3.57}$$

The current expression is similar to 1D

$$J_{dev}^i = -\frac{ie\hbar}{2m^*} \int_0^{d_i} d\xi_i \sum_{i=1}^{n} \sum_{p=1}^{max} (\sum_{m=1}^{M^i-2} c_{pm}^i \rho_p^i) \cdot 2Im[(\nabla \Phi_p^i)^* \Phi_p^i] \cdot (-\hat{n}), \tag{3.58}$$

and the current density at the lead i is

$$J_{lead}^i = -e\frac{\hbar k_D^i}{m^*} \int_0^{d_i} d\xi_i N_D(\xi_i). \tag{3.59}$$

Solve the Poisson equation and update the potential in the Schrödinger equation and repeat the iteration by Newton Method as defined in 1D until the ballistic solution is found.

3.2.2 Scattering

Applying the same PME approach in 1D, we can discretize the energy and calculate the scattering rate in k-space using Fermi golden rule, inelastic dissipative scattering characteristics can be therefore obtained.

CHAPTER 4

APPLICATION OF PME IN 1D DEVICES

4.1 *n*-*i*-*n*

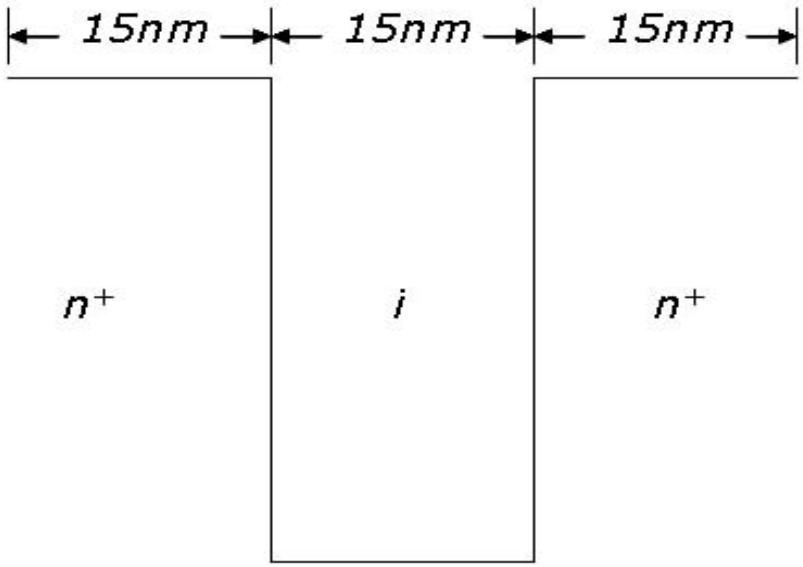

Figure 4.1. Illustration of 1D *n*-*i*-*n* device.

As shown in Fig. 4.1 the *n*-*i*-*n* resistor is composed of three parts: two highly doped silicon ($10^{20} cm^{-3}$) at two sides, in between is the intrinsic region. Each region has the same length 15nm. A uniform mesh is built along the device with a step $\Delta x = 0.25nm$, which yields 180 elements and 181 nodes. Single effective mass $m^* = 0.98m_0$ is used. Temperature is fixed at 300K. Scattering processes included are optical phonon absorbtion and emission, and acoustic phonon scattering.

Figure 4.2 shows the I-V characteristics when the device is working under bias ranging from 0 to 0.5V with a step 0.05V. Both ballistic and scattering solutions are

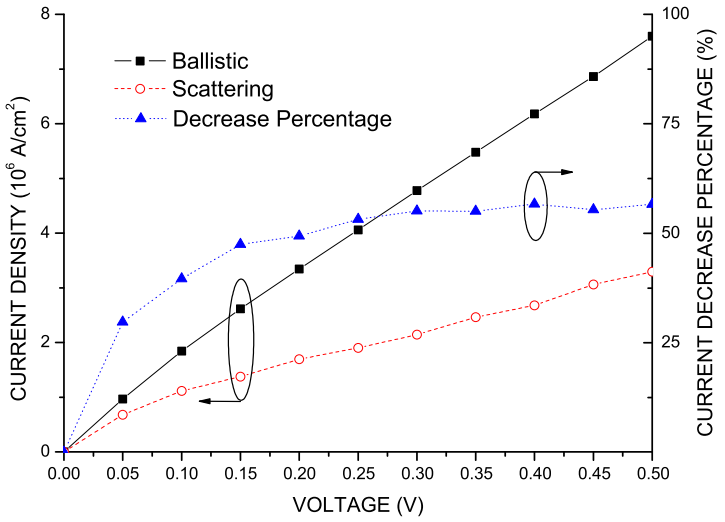

Figure 4.2. Comparison of the calculated I-V characteristics of a 1D *n*-*i*-*n* resistor operating ballistically (solid square symbols, solid black line) and with phonon scattering (open circle symbols, dashed red line). The scattering-induced percentage reduction of the current is shown by the solid triangle symbols, dotted blue line.

given. Scattering induced current decrease is very obvious and almost as high as 60% at high bias. This can be verified by checking the drift velocity along the device as shown in Fig. 4.3. Velocity is greatly reduced in the presence of scattering comparing to its ballistic value.

Figure 4.4 plots the current occupation versus energy at the bias 0.5V. It also illustrates the decrease of current. We can see that current starts to increase at energy $E_p = 0$. This current is due to electrons tunneling though the potential barrier from cathode to anode. As E_p increases, the tunneling barrier appesrs to be smaller, so the current increases very fast. At a certain point, electrons with high kinetic energy can directly transport from cathode to anode. This contribution of current, although those electrons have high velocity, will eventually decrease because of the low occupation when energy goes high.

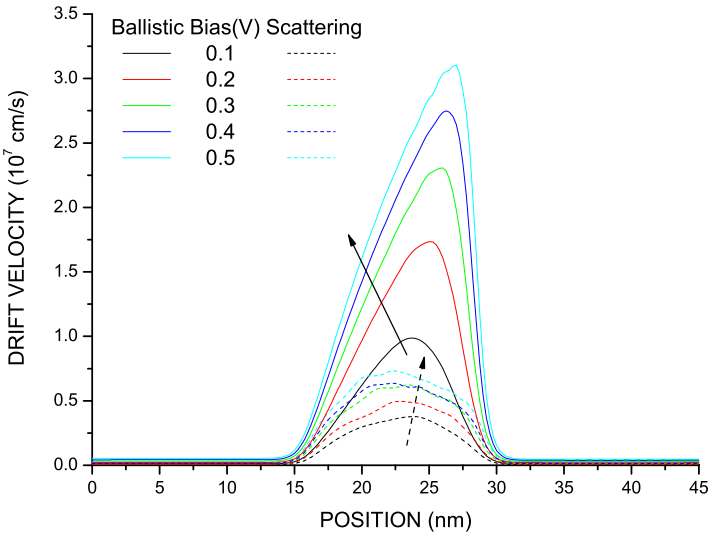

Figure 4.3. Comparison of velocity along the device in the ballistic limit (solid lines) and in the scattering limit (dash lines) under different bias. Arrow direction shows the bias increases.

In Fig. 4.5 the electron density and potential energy when the device is operating at the bias voltage 0.5V are shown with and without scattering. As we can see, the electron density does not change too much except a little increase at the right side of original intrinsic region. This change feeds back to the poisson equation will cause slight increase of the potential barrier, which leads the decrease of current.

This increase of electron density can be well explained in Fig. 4.6. The solid black and open rectangular dots show the electron occupation at the anode and cathode respectively in the ballistic case at the bias 0.5V. They satisfy the usual Fermi-Dirac distribution. Note the open black rectangular dots are a little bit irregular but the net effect does satisfy, the same reason explained and showed in Fig. 3.2. Due to the scattering processes, higher energy of anode states which originally few occupied will be occupied by hot electrons from cathode although back scattering also happens. The occupation of the cathode states almost remains the same because they are mainly filled up by the cathode contact. More direct real space illustration of this

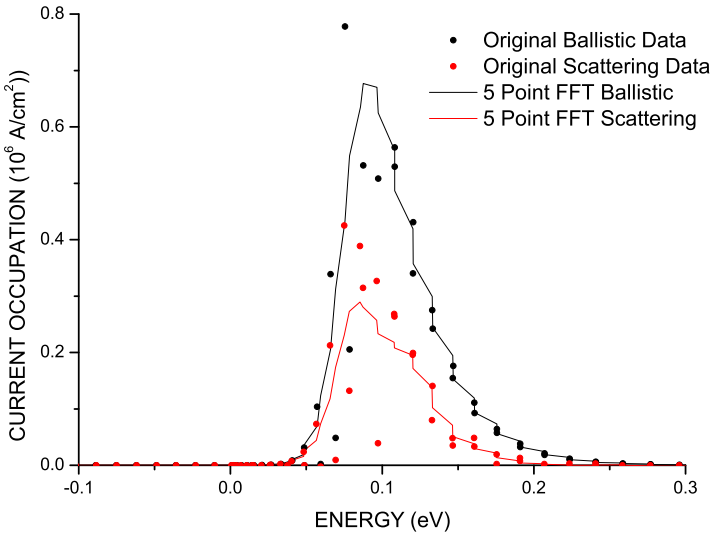

Figure 4.4. Ballistic current and scattering current occupation comparison at the bias voltage 0.5V.

phenomenon is plotted in Fig. 4.7, which compares the energy spectrum of the ballistic coherence transport and non coherent scattering transport [13].

4.2 Double-Barrier Resonant Tunneling Diode

The second 1D structure we have studied is a Si DBRTD with the following dimensions: 10.0(n)-0.5(SiO_2)-2.0(i)-0.5(SiO_2)-10.0(n) (nm). n is highly doped $10^{20}cm^{-3}$. Offset of conduction band between Si and SiO_2 is 3.1eV. Figure 4.8 shows its geometry. The whole device is equally discretized into 92 elements with $\triangle x = 0.25nm$. Effective mass for Si is $m^* = 0.98m_o$ and for SiO_2 we use $m^* = 0.5m_o$. Room temperature 300K is used. Bias range is from 0 to 0.8V with a step 0.05V. Its ballistic conduction band profile is plotted at various biases in Fig. 4.9.

Figure 4.10 plots its I-V characteristic. Bistability in the ballistic and scattering are both included. Regarding bistability both the first resonant state and second resonant state are shifted lower when the applies bias is decreasing. For the first

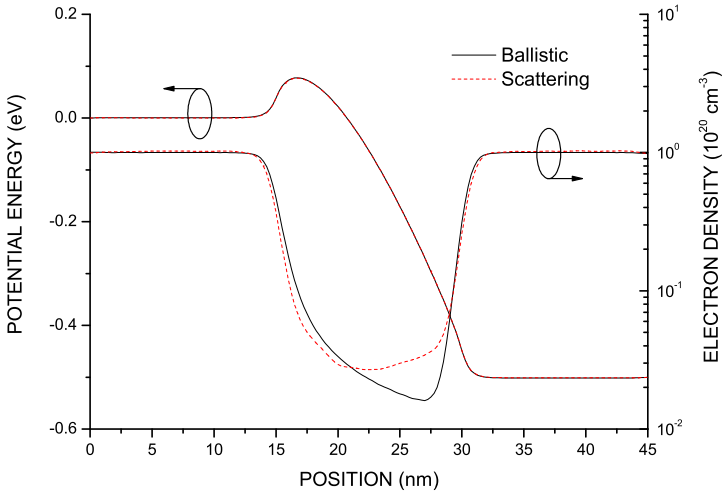

Figure 4.5. Differences of Electron density and potential energy at ballistic and scattering cases under the bias voltage 0.5V

resonant state, it shifts from 0.2V to 0.05V and the second resonant state shifts from 0.65V to 0.5V. To understand the influence of accumulation charge on bistability [14, 2], we compare the conduction band profile and electron density respectively for point (a)/(b) and (c)/(d) in Fig. 4.11. In (a) there is more electron charges accumulated in the double-barrier well than in (b), so more electrons can participate the transport, the current is higher. (c) has two electron charge bumps in the well much larger than those in (d), so the current is much higher.

It is also clear to check the energy spectrum of electron density for (c) and (d) as shown in Fig. 4.12(c) and Fig. 4.12(d). They are at the same bias, but obviously that in Fig. 4.12(c) there is a resonant state that filled up by the electrons from left. While in Fig. 4.12(d) no resonant state is occupied so there is no accumulation charge in the well. Similarly, energy spectrum of electron density for (a) and (b) are plotted in Fig. 4.12(a) and Fig. 4.12(b). There is accumulation charges in both cases as shown in Fig. 4.11(a). But it reveals that the accumulation charges are from different contacts. In Fig. 4.12(a) it is from left while in Fig. 4.12(b) it is

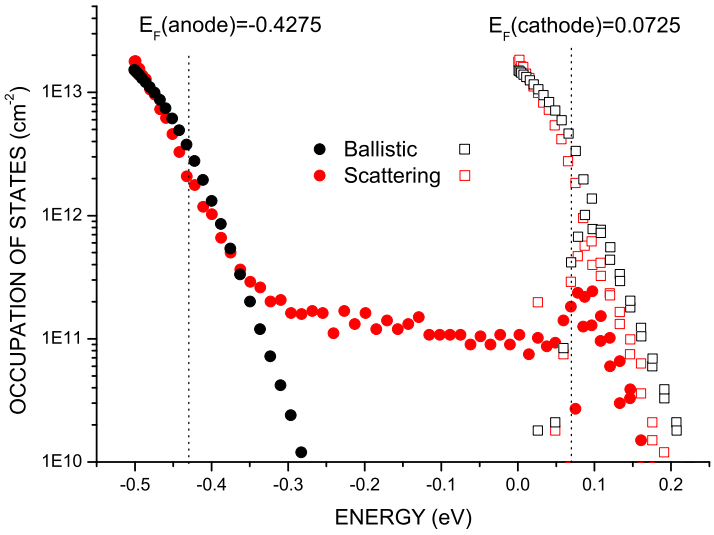

Figure 4.6. Electron density occupation versus energy without (black solid dots and open rectangular) and with scattering (red solid dots and open rectangular) at bias equals to 0.5V. Note the cathode Fermi level is not fixed at zero, instead it is fixed at $E_F(cathode) = 0.0725eV$ to make the conduction band edge to be zero at the corresponding contact, which yields the $E_F(anode) = -0.4275eV$.

due to the electron from the right. This explains the reason for bistability: following different bias history (increase or decrease), the charge occupation is different, so is the self-consistent potential energy which results in the different current density [15].

Since scattering breaks the coherence necessary to induce the resonance, scattering induced current decrease in this Si/SiO_2 RTD is tremendously large as shown in Fig. 4.10. To illustrate the effect of scattering, we compare the energy spectrum of the electron density for (e) and (f) in Fig. 4.12(e) and Fig. 4.12(f). Two resonant states are occupied in both cases. The difference is that when scattering is introduced, electrons in the higher resonant state in (e) will lose energy or scattering out. On the contrary, more electrons will scatter into the lower energy state. We plot the occupation of notch states (resonant states in the notch) with and without scattering in Fig. 4.13. Note in the ballistic limit, the notch states should not be filled up

because it should totally depend on the scattering processes. This unphysical effect is used to obtain a flat potential band in the ballistic case as discussed by Frensley [9]. As we can see, scattering processes indeed increase the occupation of these states. But they are still not strong enough. Impurity and electron electron interaction may have to be also included.

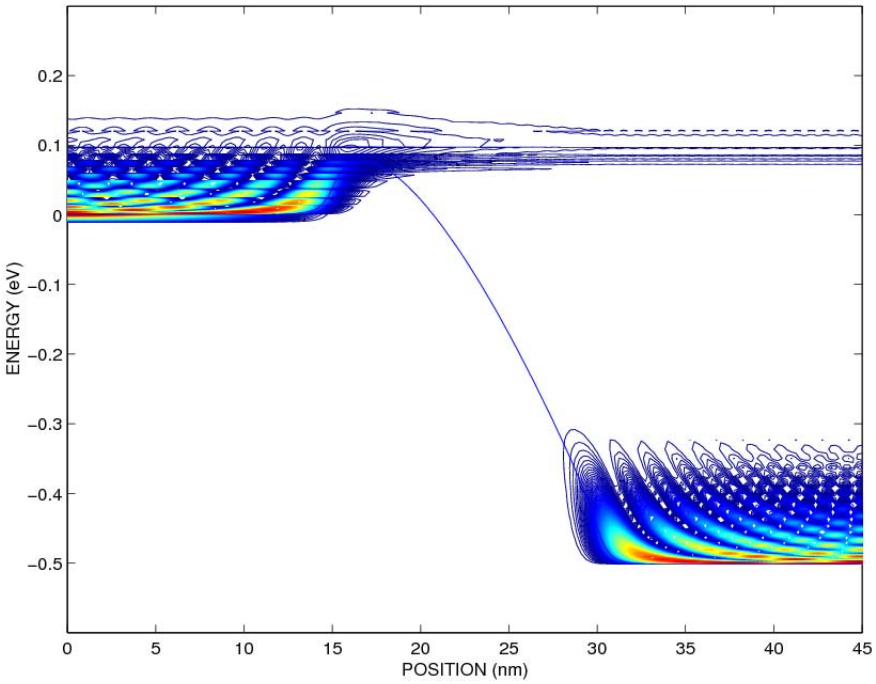

(a) Ballistic

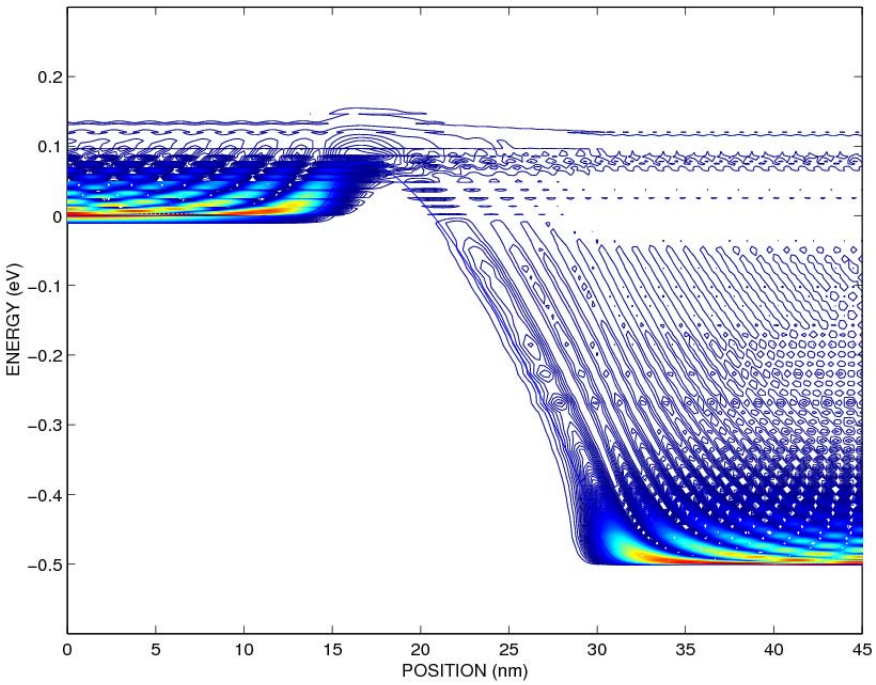

(b) Scattering

Figure 4.7. (a) and (b) show the coherent ballistic transport and noncoherent transport with the spectrally resolved electron density at bias 0.5V respectively.

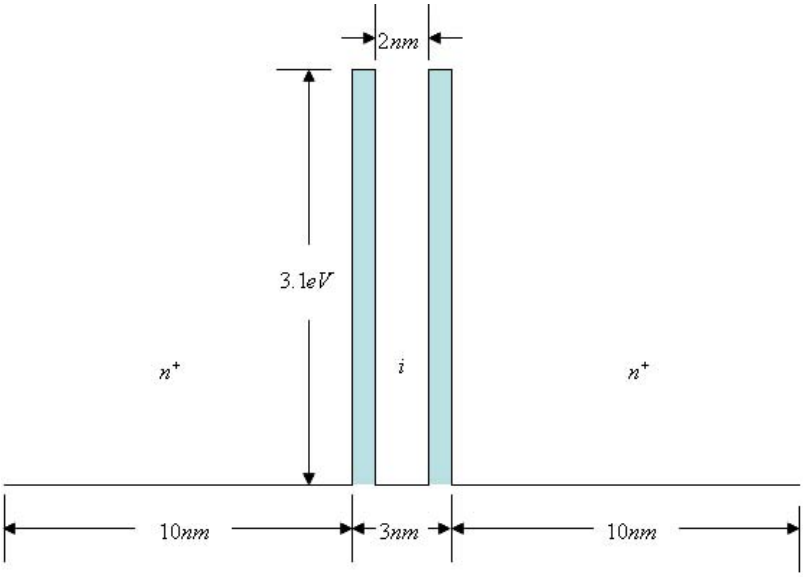

Figure 4.8. Geometry of Si/SiO_2 double barrier resonant tunneling diode.

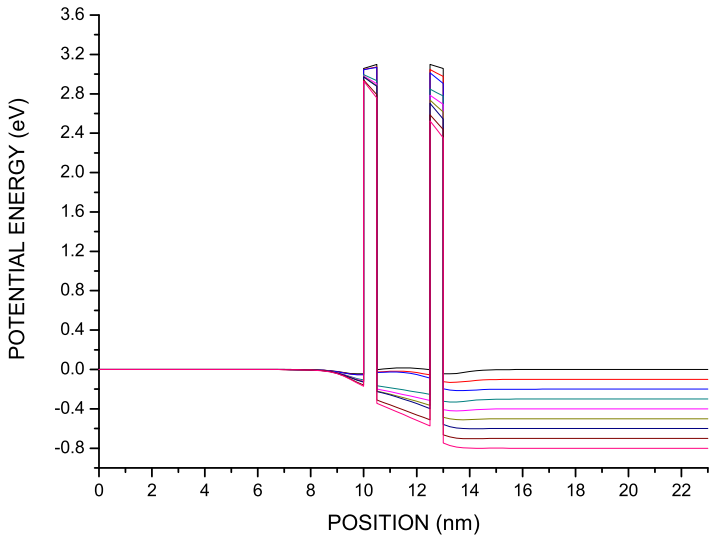

Figure 4.9. Conduction band profile of Si/SiO_2 double barrier resonant tunneling diode at various biases with an increase of 0.05V.

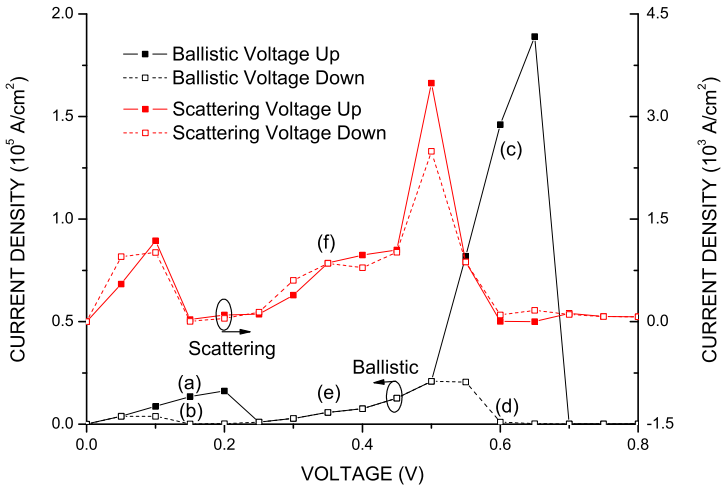

Figure 4.10. Comparison of the calculated I-V characteristics of bistability in the ballistic and scattering limit. The solid black line/solid squares show the current as the applied bias increases, while the dashed black line/open squares refer to the case of decreasing bias. The solid red lines/solid circles and dashed red lines/open circles correspond to the same increasing/decreasing bias but with the inclusion of inelastic scattering. Note scattering induced current lowing is tremendously large, currents are plotted on different scale.

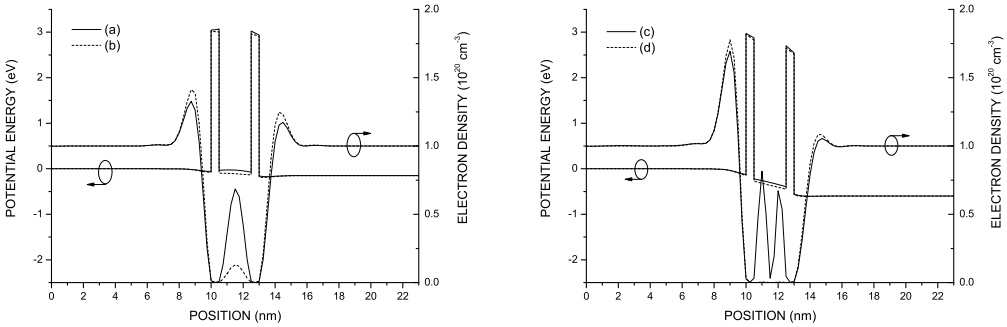

(a) Conduction band (a)/(b)

(b) Conduction band (c)/(d)

Figure 4.11. Comparison of conduction band profile and electron density of (a)/(b) and (c)/(d)

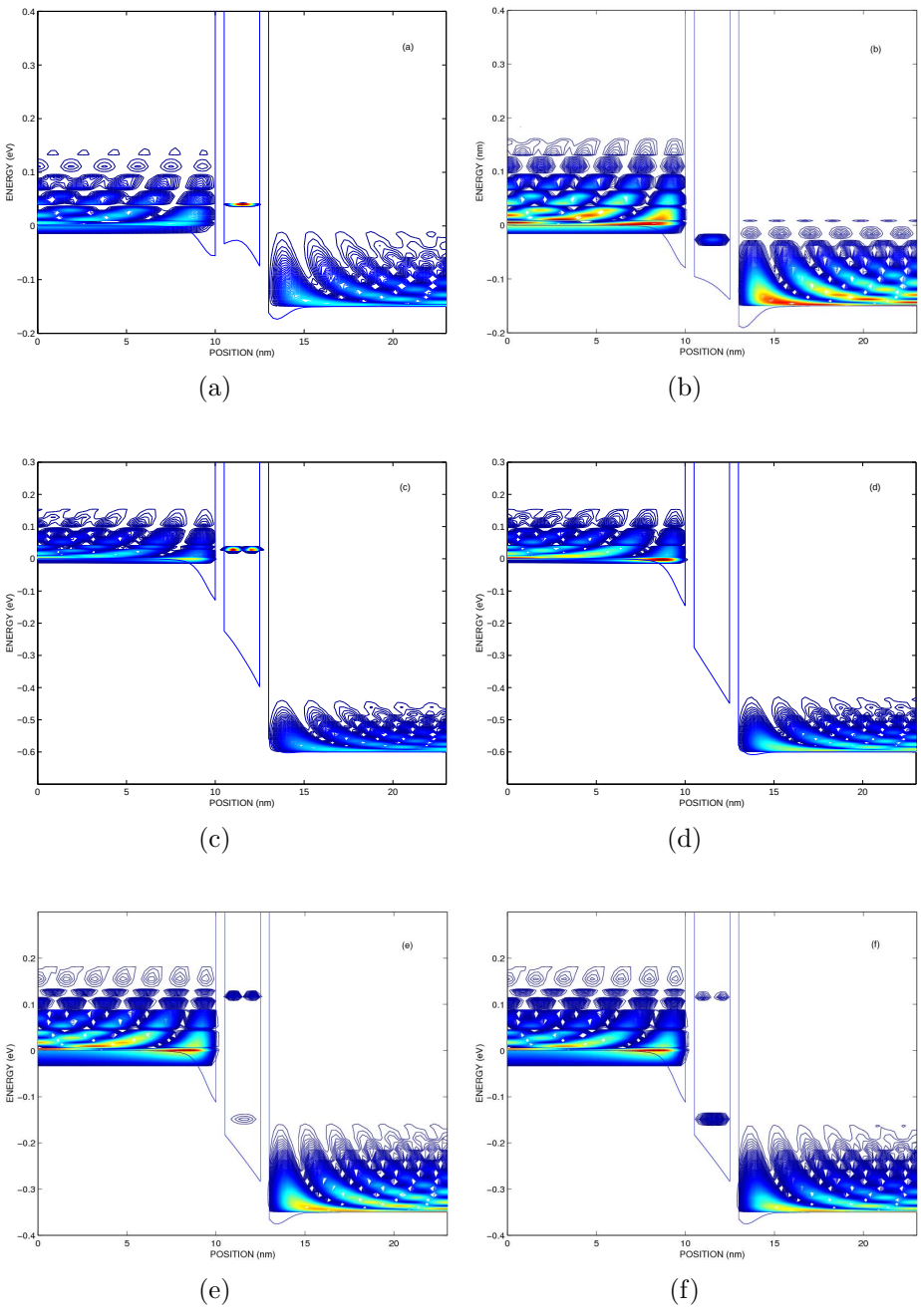

Figure 4.12. Energy spectrum of electron density of (a) (b) (c) (d) (e) and (f).

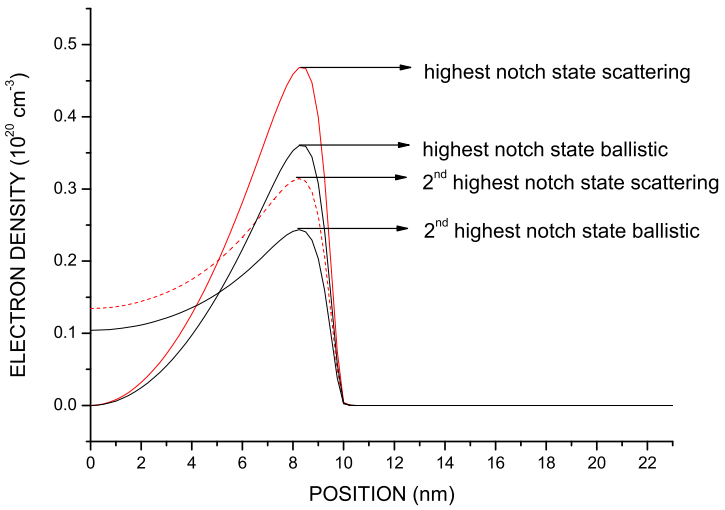

Figure 4.13. Occupation of notch states with and without scattering.

CHAPTER 5

APPLICATION OF PME IN 2D DEVICES

We simulate four double-gate Field Effect Transistors (DG-FETs) with different geometries. They are straight, taper I, taper II and dog bone. Fig. 5.1 shows their 2D triangular mesh created by EasyMesh [21].

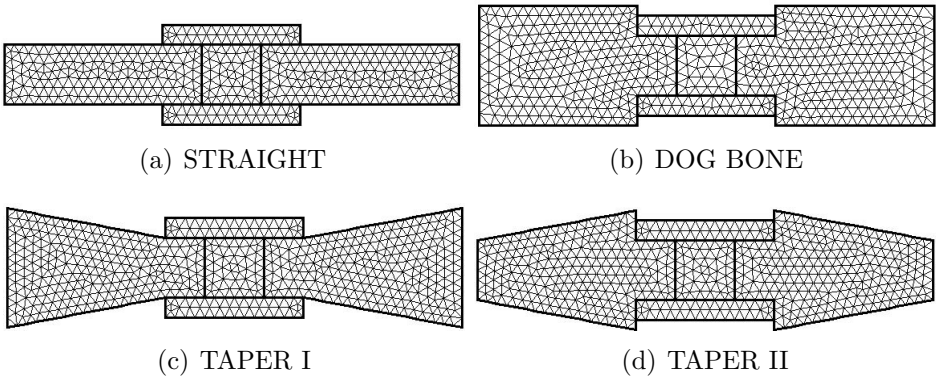

(a) STRAIGHT (b) DOG BONE

(c) TAPER I (d) TAPER II

Figure 5.1. 2D triangular meshes of various geometries.

Their specific sizes are given in Fig. 5.2. Source and drain, each being 10nm, are highly doped $10^{20} cm^{-3}$. Channel is intrinsic with a length of 3nm. Gate is 7nm long with 2nm overlap on both source and drain side. SiO_2 is 1nm thick. For the straight and taper II, the source and drain thickness is 3nm and for taper I and dog bone is 6nm. The whole simulation domain is discretized into small triangle meshes. Typical nodes number is about 500 to 600. Device operating temperature is set to 300K.

Consider the reasonably small value of the gate leakage current, in this work we ignore it by requiring the wave function to be zero at the gate contacts. Hence the gate bias is simply simulated by proper boundary conditions.

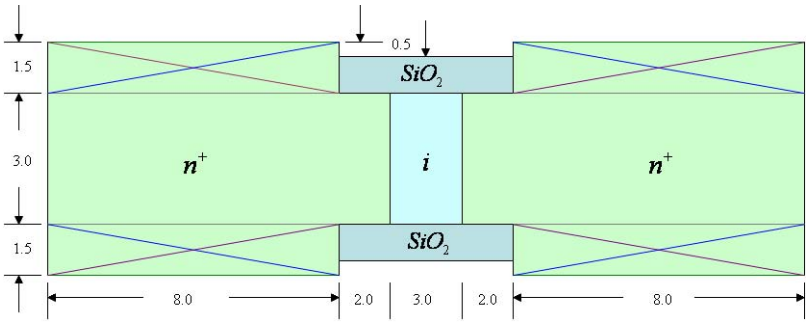

Figure 5.2. Specific sizes for four DG-FETs.

5.1 Ballistic Transport

To have a direct view of the self-consistent solution. Fig. 5.3 plots the self-consistent electron density for devices operating at $V_{GS} = 0.3V$ and $V_{DS} = 0.5V$. It is very clear that for dog bone, taper I and taper II there are strong reflections because of the geometry effects, which causes higher electron density. While for straight, no reflection is observed from the electron density. But in Fig. 5.3(a), we can see that there is a region in the source the electron density is extremely low. This effect shows that the source cannot supply enough electrons under higher bias. We can increase the region of the source (wider of longer) or reduce the overlap length of gate and source to minimize the effect [17].

Their individual drain current versus gate voltage is plotted in Fig. 5.4. As we can see for the same gate bias the straight device has the highest current, followed by the taper I, taper II and dog bone has similar result. From semiclassical perspective, we expect the dog bone has the highest current and then the taper I and II be the same, the current for the straight should be the minimum because semiclassical resistance is defined as $R = \rho l/s$: dog bone is the widest, the straight is the thinnest, taper I and II are the same in the middle. To correctly explain this phonomenom we have to include quantum resistance [27, 17]. For the straight, incoming waves transport through the device directly without any reflection. But for other geometries, reflections happen in the device more or less as shown in the electron density. This reflection induced

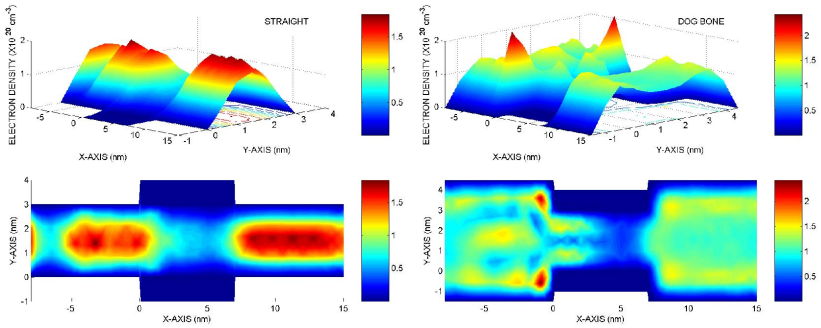

(a) STRAIGHT (b) DOG BONE

(c) TAPER I (d) TAPER II

Figure 5.3. Electron density for all DGFETs operating at $V_{GS} = 0.3V$, $V_{DS} = 0.5V$.

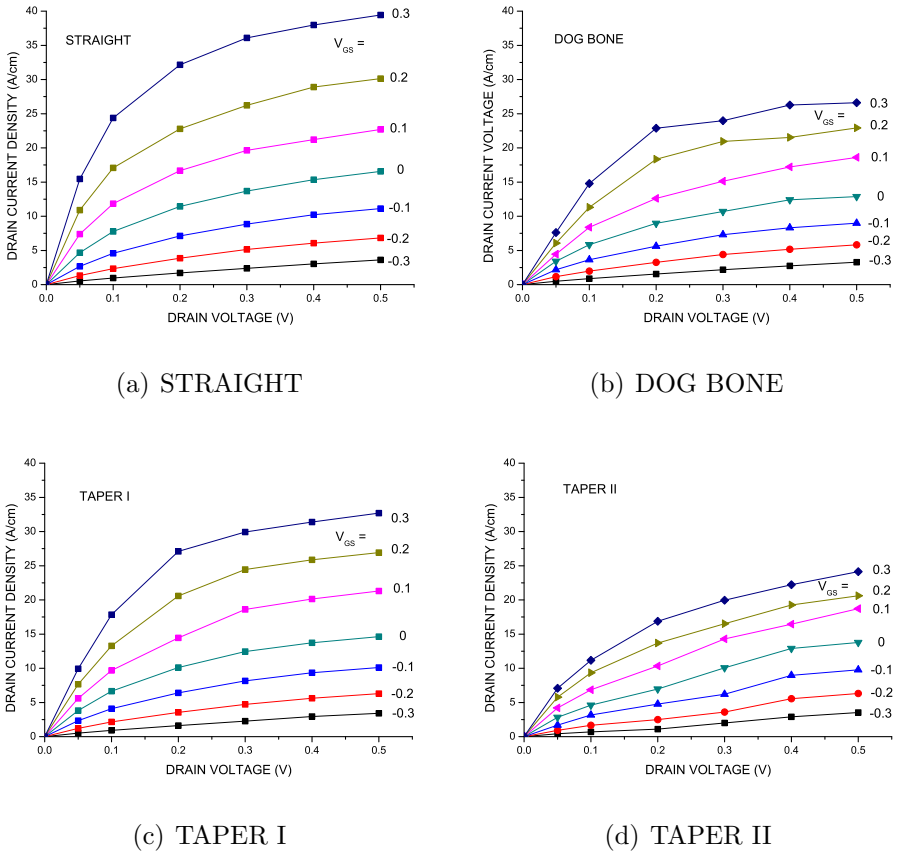

(a) STRAIGHT (b) DOG BONE

(c) TAPER I (d) TAPER II

Figure 5.4. I_{DS}-V_{DS} in the ballistic limit.

quantum resistance which is comparable to the semiclassical resistance has to be taken into account in order to correctly explain the current characteristic.

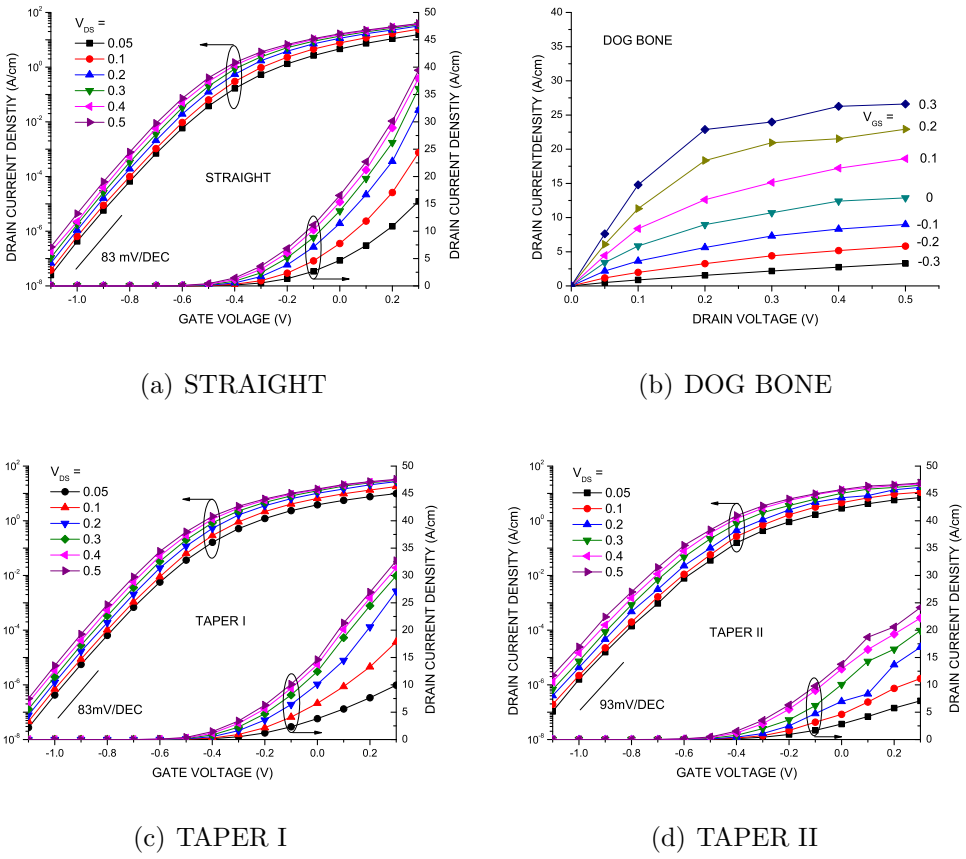

(a) STRAIGHT (b) DOG BONE

(c) TAPER I (d) TAPER II

Figure 5.5. I_{DS}-V_{GS} in the ballistic limit.

To study the subthreshold gate control, I_{DS}-V_{GS} for each device is plotted in Fig. 5.5. Taper II and dog bone show a higher subthreshold slop 93mV/Dec compared with the straight and taper I 83mV/Dec. Note this simulation result is different from Laux' because we deliberately shrink the size of the devices (length and width). Not only our subthreshold slop is higher than his, but also the difference between dog bone/taper II and straight/taper I is distinguishable.

To illustrate the effect of gate control, we plot the line electron density along the transport direction by doing the integral of the 1D cross section. The result when the

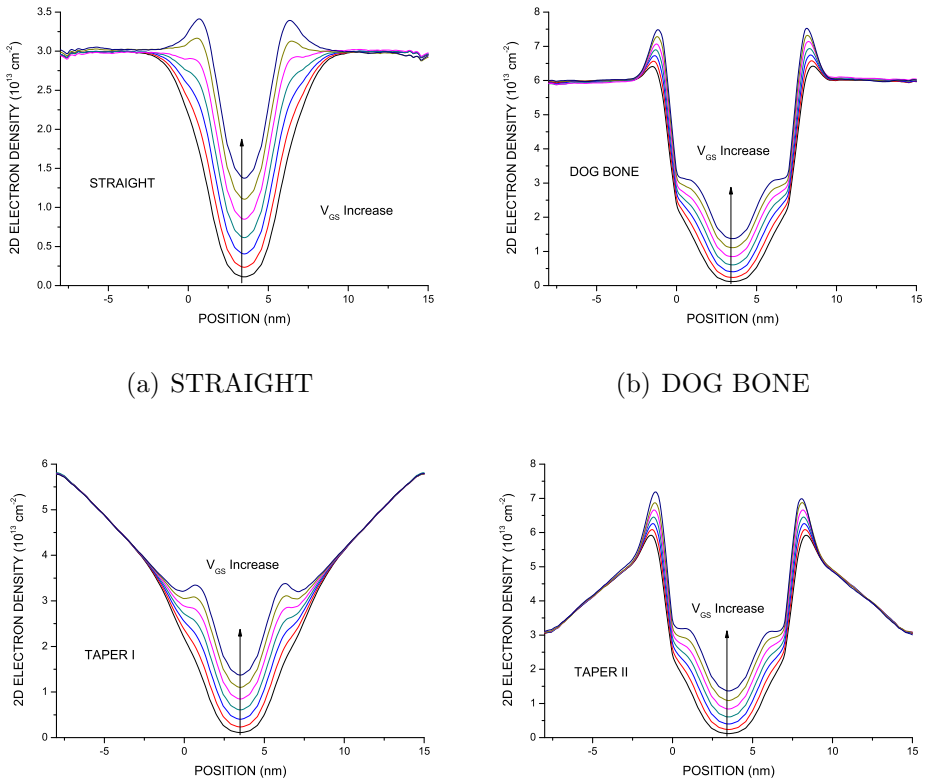

(a) STRAIGHT

(b) DOG BONE

(c) TAPER I

(d) TAPER II

Figure 5.6. Line electron density (integral of cross section) along transport direction for DGFETs.

device is in equilibrium is given in Fig. 5.6. As gate bias increases, the conduction band at the gate is pulling downward and the electron density is increasing. More electrons will accumulate in the channel. When source-drain bias is applied, more electrons can participate the transport, hence larger current is obtained.

5.2 Cone Barriers

We add upward cone-like barriers in the Hartree potential to mimic the effect of the ionized impurities. Fig. 5.7 shows one situation of the self-consistent potential when 5 barriers are introduced. The cone has a height of 0.3eV and a radius 0.5nm. Scatters are placed randomly on the source region. Fig. 5.8 is the corresponding electron density.

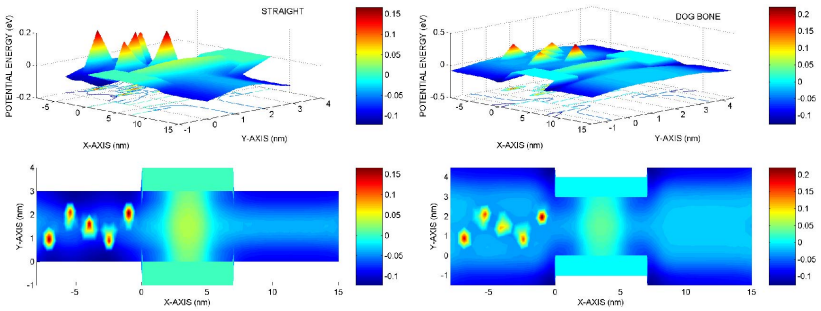

(a) STRAIGHT (b) DOG BONE

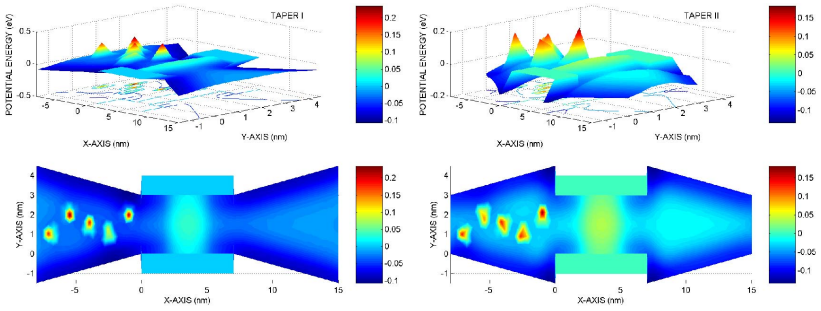

(c) TAPER I (d) TAPER II

Figure 5.7. Potential energy when five cone barriers are introduced in the Hartree potential of DGFETs at equilibrium.

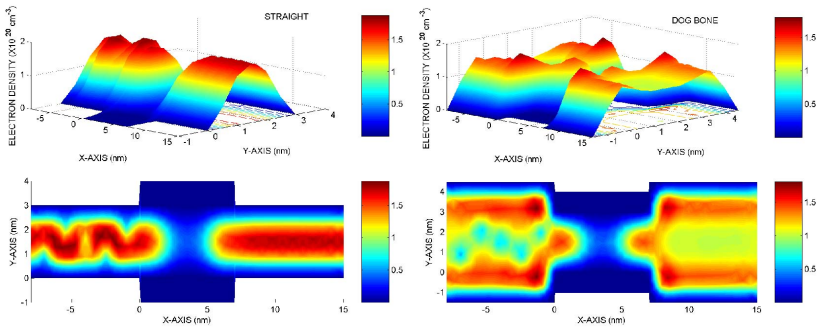

(a) STRAIGHT

(b) DOG BONE

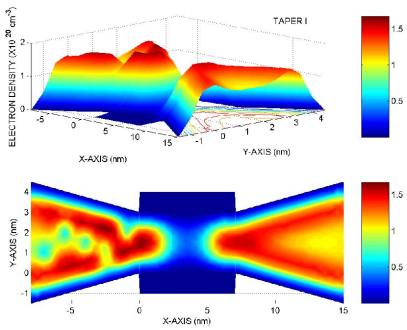

(c) TAPER I

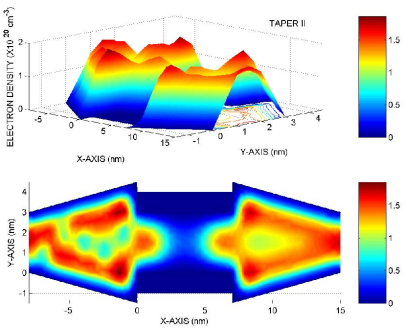

(d) TAPER II

Figure 5.8. Electron density when five cone barriers are introduced in the Hartree potential of DGFETs at equilibrium.

To evaluate the effect of cone barriers on the I_{DS}-V_{DS} characteristics statistically, we run the simulation 4 times with different random placement and average the results as shown in Fig. 5.9. Color dots represent the current value under different barriers placement. Solid black line is the ballistic case and the dashed red line is the average result for the scattering. The fact that current reduction due to scattering is very obvious.

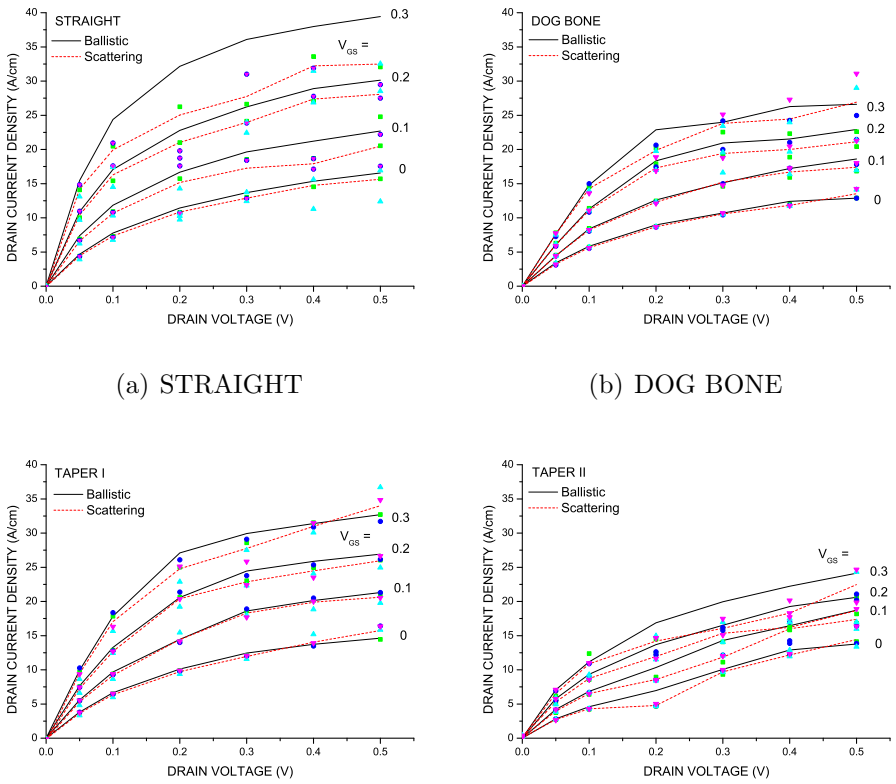

(a) STRAIGHT (b) DOG BONE

(c) TAPER I (d) TAPER II

Figure 5.9. Calculated I_{DS}-V_{DS} characteristics at various V_{GS} in the ballistic limit (solid black line) and in the cone barriers (dashed red line) with five random distribution of dopants in the source averaged from four different spatial configurations (different shape and color dots).

5.3 Ionized Dopants

Although the cone barrier method can capture the way ionized dopants scattering affects the current, it is limited to just an intuitive evaluation due to the following facts: we choose a cone-like barrier to simplify the real screening potential; the number of scatters is chosen arbitrarily; the hight and width of cone is also chosen without any theoretical justification; where to put those scatters is an statical process which cannot be handled easily. More accurate solution accounts for impurity scattering can be achieved by replacing the evenly distributed dopant with singular dopant charges, following the work by Gilbert and Ferry [10]. In our 2D simulations, these scatterers consist of line charges with linear density ($\sim e/L_{TF}$, where L_{TF} is the Thomas-Fermi screening length) and areal density required to mimic the effect of the ionized dopants. These centers constitute non-phase-breaking scatterers, decoherence and dissipation emerging only after performing an average over their configurations [16].

Singular charges can be expressed as a delta function $\delta(x_i, y_i)$, numerically in FEM this can be interpolated as a small region (S_i) composed by certain triangles including the desired node i. For all the scatters introduced, charge neutrality equation has to be satisfied: $\int_S N_d(x,y)ds = \int_S \delta(x_i,y_i)dS \approx \sum_i \int_{S_i} N_d^i(S_i)dS_i$. After evenly distributed dopants have been replaced by singular charges, impurity scattering with screening effect can be automatically included in our solution in the same frame work as the ballistic case.

We put ten scatters in the devices, five in the source region and five in the drain, no charges in the intrinsic channel. Fig. 5.10 is the obtained self-consistent conduction band profile for straight, dog bone and taper at equilibrium. Dopants are positive charges in the device which causes the downward spikes in the conduction band. Meanwhile electrons are attracted and piled up in the charge region as shown in Fig. 5.11. There are quantum interference effect between singular charges especially for two pairs of them which have the same x-axis as we can see that their potential

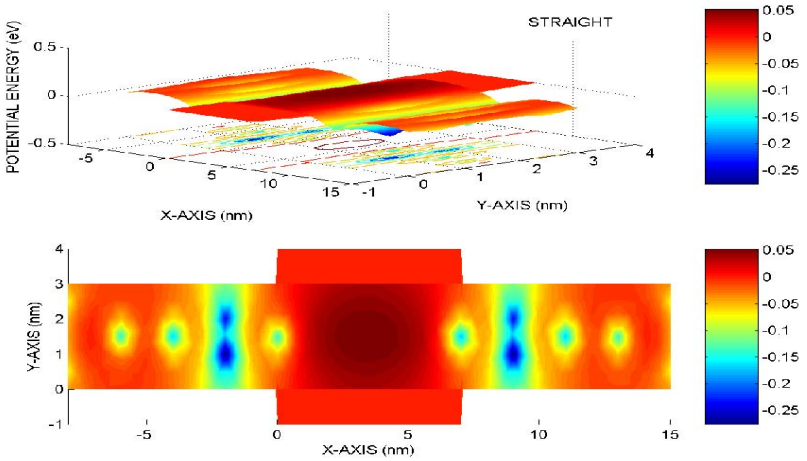

(a) STRAIGHT

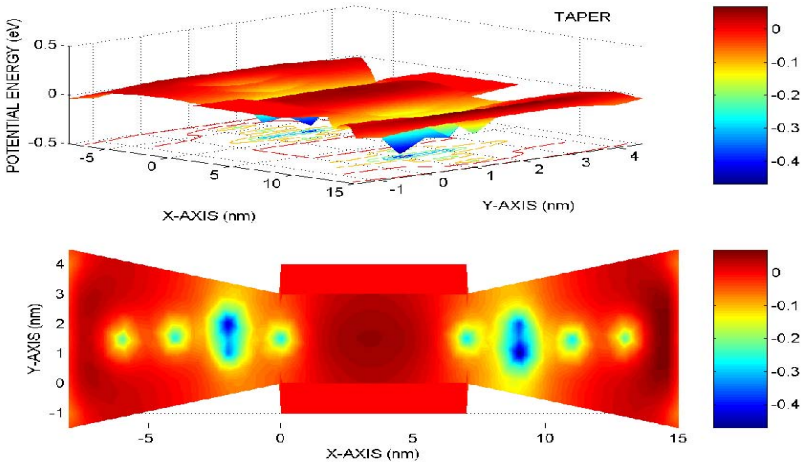

(b) TAPER

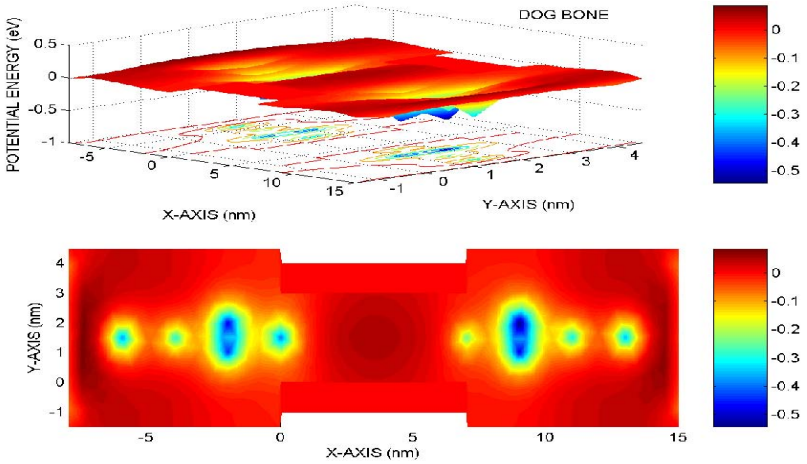

(c) DOG BONE

Figure 5.10. Calculated conduction band profile at equilibrium in DGFETs with ten 'dopants' introduced at random positions in the source and drain region of the devices.

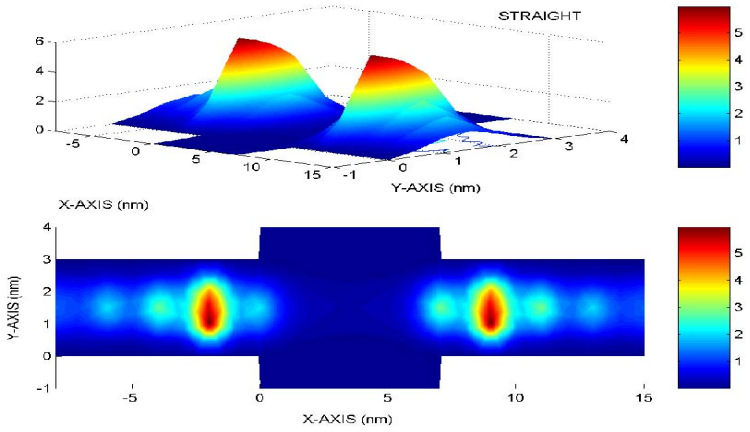

(a) STRAIGHT

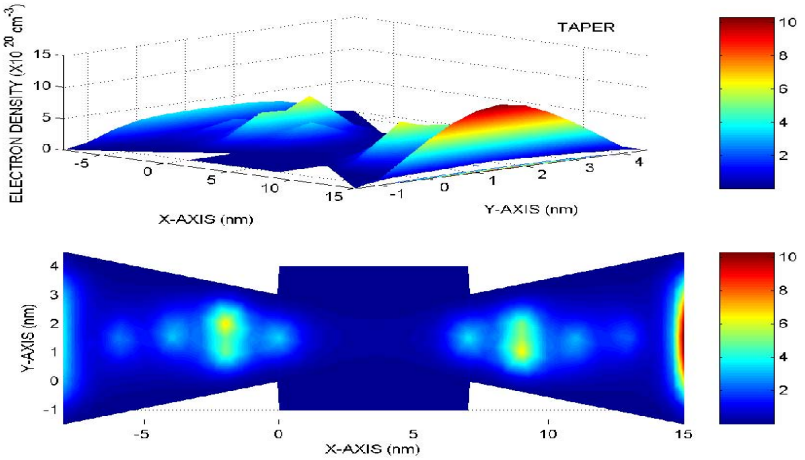

(b) TAPER

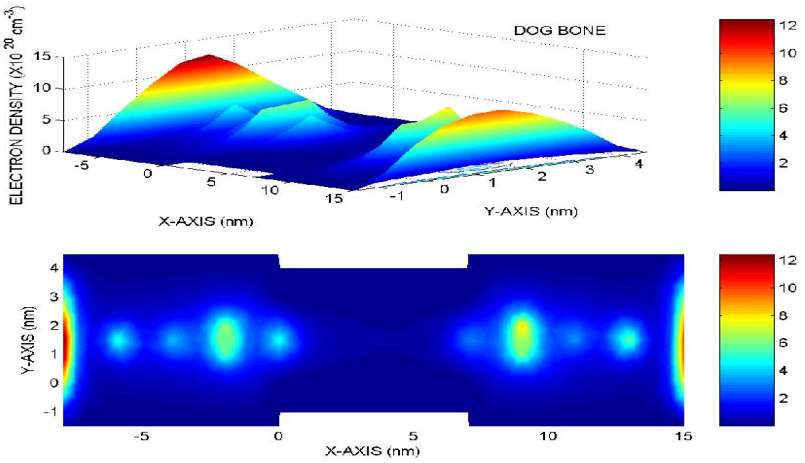

(c) DOG BONE

Figure 5.11. Electron density at equilibrium in DGFETs with ten 'dopants' introduced at random positions in the source and drain region of the devices.

and electron density spikes are not separated. We can cut the device along the line and plot the energy spectrum. Figure 5.12 plots the energy spectrum of the cross section at position x=-2.0nm of device Taper at V_{GS}=0V, V_{DS}=0.5V. Clearly, there is a resonant states between them. The barrier potential is not the same for the two dopants are due to the fact there our implementation of delta function still relies on the irregular 2D mesh.

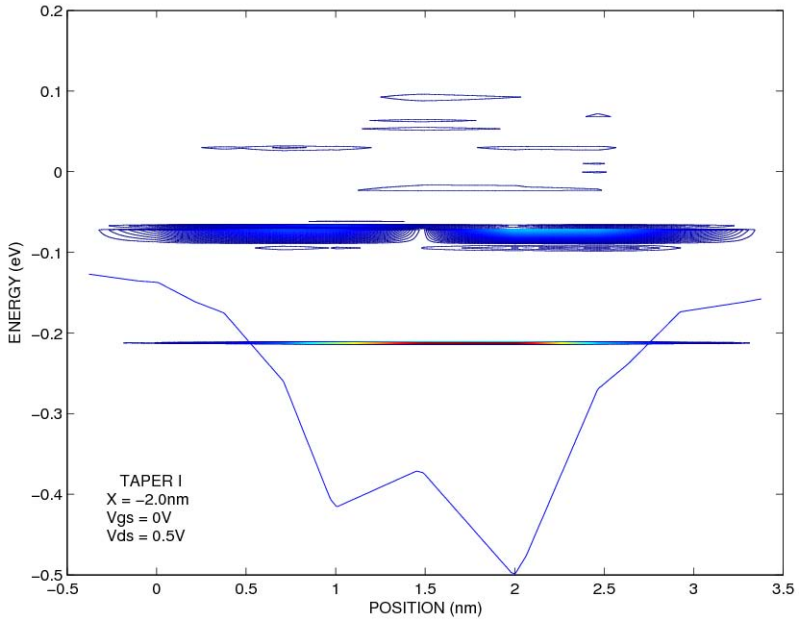

Figure 5.12. Energy spectrum of the cross section at position x=-2.0nm of Taper at V_{GS}=0V, V_{DS}=0.5V.

As in the cone-like barriers, having calculated the current-voltage characteristics for one configuration of our pseudo-dopants, we have repeated the process for 4 different random configurations and have averaged the currents to obtain the I_{DS}-V_{DS} characteristics shown in Fig. 5.13. We can see that at this scale, fluctuation of current (color dots) under different spatial dopant configurations is large. The average currents of the three devices clearly show that the influence of pure geometrical effects are greatly reduced in the presence of ionized impurity scattering. Of intetest is also the observation that for some configurations the current in the presence of

dopants can exceed the ballistic current. This is due to the existence of resonant states in the screening potential well as shown in Fig. 5.12. This has been discussed by Gilbert and Ferry [10], who showed that discrete dopants modify the potential profile so drastically that resonant levels may induce 'spikes' in the current-voltage characteristics. To clearly visualize how the resonant states in the device introduced by the ionized scatters affect the I_{DS}-V_{DS} characteristics, we set a small V_{DS} step (0.01V) that resonant levels induce 'spikes' in the current-voltage characteristics as shown in Fig. 5.14.

5.4 Dissipative Transport - Pauli Master Equation

Finally we have applied the PME framework to the study of transport in the presence of optical and acoustic phonon scattering in 2D. The results, illustrated by the I_{DS}-V_{DS} characteristics in Fig. 5.15, show that, similarly to what found in the ballistic case, the straight geometry yields the largest current, the dog-bone geometry the smallest. However, both the magnitude of the current as well as the difference caused by the various geometries are greatly reduced. This is due to the fact that scattering processes destroy the electron coherence and so reduce – but do not eliminate it altogether – the effects caused by the access geometry. In conclusion, the access geometry is still found to play a role in mesoscopic device design, although scattering (both phase-breaking and non-phase-breaking) reduces its importance.

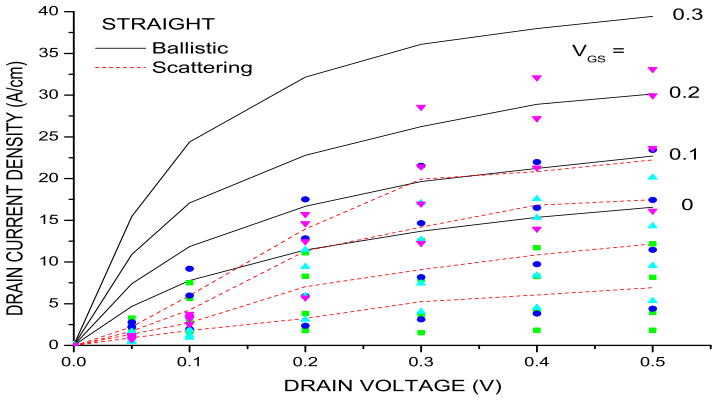

(a) STRAIGHT

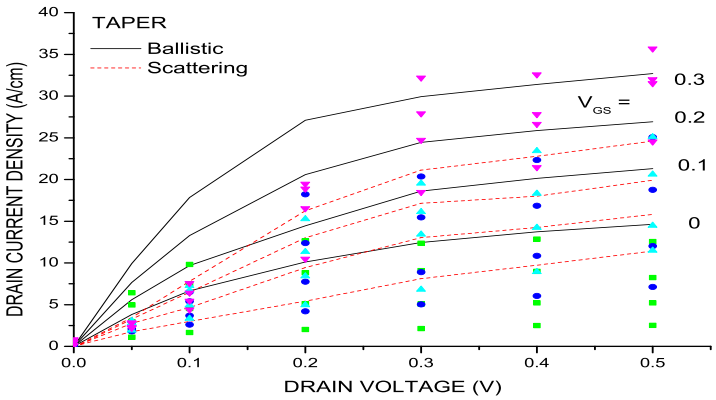

(b) TAPER

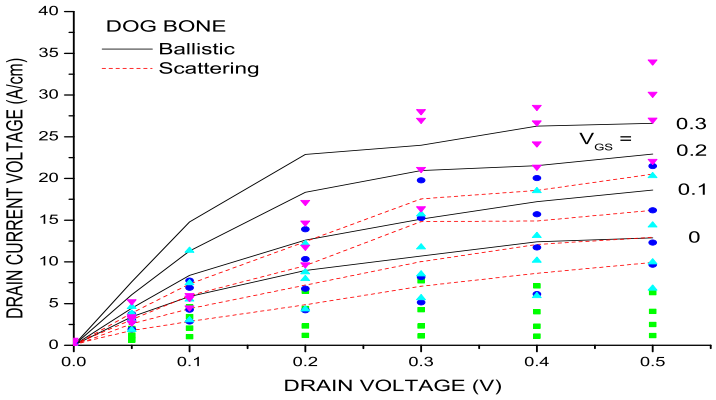

(c) DOG BONE

Figure 5.13. Calculated I_{DS}-V_{DS} characteristics at various V_{GS} in the ballistic limit (solid black line) and in the impurity scattering limit (dashed red line) with ten random distribution of dopants averaged from four different spatial configurations of the dopants (different shape and color dots).

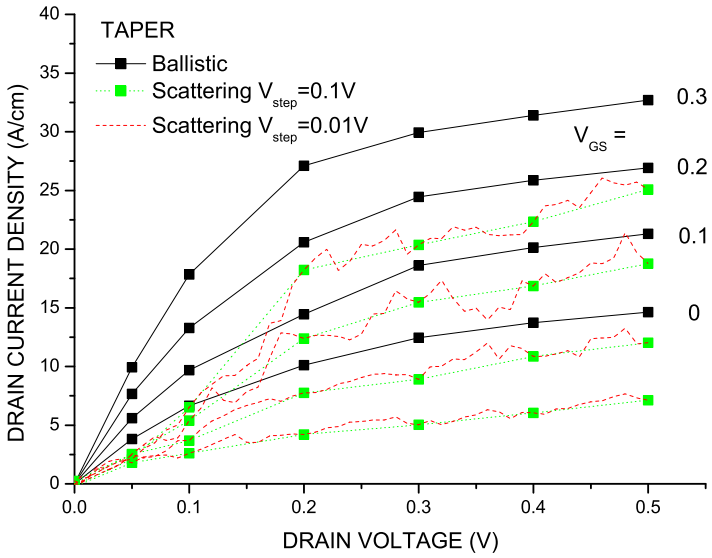

Figure 5.14. I_{DS}-V_{DS} characteristics at various V_{GS} in the ballistic limit (solid black line, solid black squares) and in the impurity scattering limit (dashed green line, solid green squares) ΔV_{GS}=0.1V, (solid red line) ΔV_{GS}=0.01V.

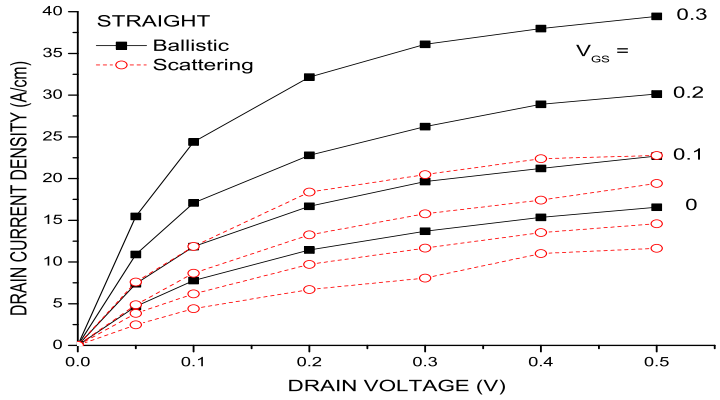

(a) STRAIGHT

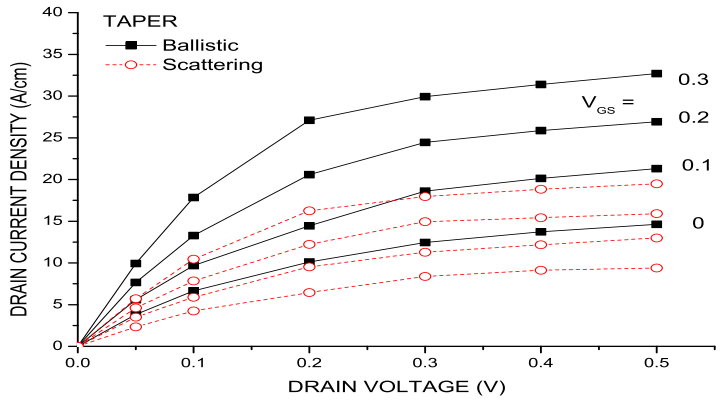

(b) TAPER

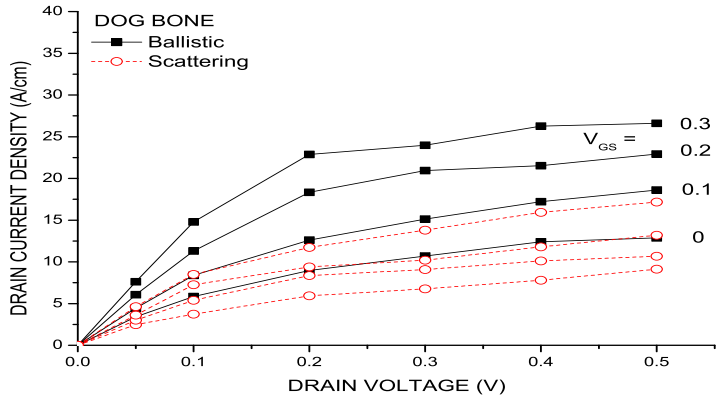

(c) DOG BONE

Figure 5.15. I_{DS}-V_{DS} at various V_{GS} in the ballistic limit (solid black line) and in the scattering limit (dashed red line) using Pauli Master Equation.

CHAPTER 6

CONCLUSION

We have studied dissipative quantum transport in 1D by solving the Pauli Master Equation in a simple isotropic effective-mass approximation self-consistently with Poisson equation. We have found that, not surprisingly, phonon scattering reduces current of n-i-n resistors by as much as 60%. Also, because of the loss of the coherence required to build up the resonance, the current of a double-barrier RTD is greatly reduced and the bistability is less obvious in the presence of scattering. We have also evaluated the effect of ionized dopants and phonon scattering on the access resistance of thin body DGFETs of various access geometries using 2D simulations. Our results show that 1. ionized dopants in the source (and drain) regions cause large 'fluctuations' of the current but their configuration-average tends to reduce the role played by geometrical effects; 2. phase-breaking phonon scattering also reduces the geometrical effects to some extent, albeit not completely.

APPENDIX A

SCATTERING RATES

We have included nonpolar scattering with optical phonons and acoustic phonons. Their scattering rates $1/\tau_{\mu i}^{nop}(\vec{k})$ and $1/\tau_{\mu i}^{nac}(\vec{k})$ are given below [6].

1. Nonpolar Optical Phonons Scattering

$$\frac{1}{\tau_{\mu i}^{nop}(\vec{k})} = \frac{m^*(DK)_{op}^2}{2\hbar^2\rho_x\omega_{op}} \left\{ \begin{array}{c} N_{op} \\ N_{op}+1 \end{array} \right\} \sum_{\nu i'} \theta \left\{ \begin{array}{c} E_\nu(\vec{k'}) - E_\mu(\vec{k}) + \hbar\omega_{op} \\ E_\nu(\vec{k'}) - E_\mu(\vec{k}) - \hbar\omega_{op} \end{array} \right\} F_{\nu i',\mu i} \tag{A.1}$$

where $(DK)_{op}$ is the deformation potential, ρ_x the crystal density, $\hbar\omega_{op}$ the phonon energy, $N_{op} = 1/exp[\hbar\omega_{op}/(k_BT)]$ the Bose-Einstein phonon occupation number, the upper line in the parenthesis corresponding to phonon absorptions, lower line corresponding to phonon emissions. Step function equals to 1 when variable is great than 0 or 0 when smaller than 0. $F_{\nu i',\mu i}$ is the form factor

$$F_{\nu i',\mu i} = \int_\Omega ds |\Phi_\nu^{i'}(x,y)|^2 |\Phi_\mu^i(x,y)|^2 \tag{A.2}$$

measuring the overlap of wave functions.

2. Nonpolar Acoustic Phonons Scattering

$$\frac{1}{\tau_{\mu i}^{nac}(\vec{k})} = \frac{m^*\Delta_{ac}^2 k_B T}{2\hbar^3\rho_x c_s^2} \sum_{\nu i'} \theta[E_\nu(\vec{k'}) - E_\mu(\vec{k})] F_{\nu i',\mu i}. \tag{A.3}$$

where Δ_{ac} is the acoustic deformation potential and c_s is the average sound velocity.

APPENDIX B

OBSERVABLES

We use electron density to evaluate the observables of interest. For an observable O, its expectation value is given by [6]

$$< O >= \frac{Tr(\rho O)}{Tr(\rho)} \tag{B.1}$$

The kinetic energy can be therefore expressed

$$< E_{kin}(\vec{r}) >= \frac{\sum_{\mu\vec{k}i} \rho_{\mu\vec{k}i}[E_\mu(\vec{k}) - E_c(\vec{r})]|\Phi^i_\mu(\vec{r})|^2}{\sum_{\mu\vec{k}i} \rho_{\mu\vec{k}i}|\Phi^i_\mu(\vec{r})|^2} \tag{B.2}$$

where $E_c(\vec{r})$ is the conduction band. Similarly, we can have the expression for the velocity. The current is determined by $\vec{J} = -enV$, so the velocity can be calculated

$$< V(\vec{r}) >= \frac{\sum_{\mu\vec{k}i} \rho_{\mu\vec{k}i}(-\frac{ei\hbar}{2m^*})[(\nabla\Phi^i_\mu(\vec{r}))^*\Phi^i_\mu(\vec{r}) - \Phi^i_\mu(\vec{r})^*(\nabla\Phi^i_\mu(\vec{r}))]}{\sum_{\mu\vec{k}i}(-e\rho_{\mu\vec{k}i})\Phi^i_\mu(\vec{r})\Phi^i_\mu(\vec{r})^*} \tag{B.3}$$

BIBLIOGRAPHY

[1] Büttiker, M. Four-terminal phase-coherent conductance. *Phys. Rev. Lett. 57*, 14 (Oct 1986), 1761–1764.

[2] Cahay, M., McLennan, M., Datta, S., and Lundstrom, M. S. Importance of space-charge effects in resonant tunneling devices. *Applied Physics Letters 50*, 10 (1987), 612–614.

[3] Dahlquist, Germund. *Numerical Methods*. Prentice-Hall, 1974.

[4] Datta, Supriyo. *Electronic Transport In Mesoscopic Systems*. Cambridge University Press, 1995.

[5] Datta, Supriyo. *Quantum Transport: Atom to Transistor*. Cambridge University Press, 2005.

[6] Fischetti, M. V. Theory of electron transport in small semiconductor devices using the Pauli master equation. *Journal of Applied Physics 83* (Jan. 1998), 270–291.

[7] Fischetti, M. V. Master-equation approach to the study of electronic transport in small semiconductor devices. *Journal of Applied Physics 59* (Feb. 1999), 4901–4917.

[8] Fischetti, Massimo V., and Laux, Steven E. Monte carlo analysis of electron transport in small semiconductor devices including band-structure and space-charge effects. *Phys. Rev. B 38*, 14 (Nov 1988), 9721–9745.

[9] Frensley, William R. Boundary conditions for open quantum systems driven far from equilibrium. *Rev. Mod. Phys. 62*, 3 (Jul 1990), 745–791.

[10] Gilbert, M. J., and Ferry, D. K. Vorticity and Quantum Interference in Ultra-Small SOI MOSFETs. *IEEE Transactions on Nanotechnology 4* (May 2005), 355–359.

[11] Jacoboni, C., and Reggiani, L. The Monte Carlo method for the solution of charge transport in semiconductors with applications to covalent materials. *Reviews of Modern Physics 55* (July 1983), 645–705.

[12] Jin, Seonghoon, Fischetti, Massimo V., and wei Tang, Ting. Modeling of electron mobility in gated silicon nanowires at room temperature: Surface roughness scattering, dielectric screening, and band nonparabolicity. *Journal of Applied Physics 102*, 8 (2007), 083715.

[13] Jin, Seonghoon, Park, Young June, and Min, Hong Shick. A three-dimensional simulation of quantum transport in silicon nanowire transistor in the presence of electron-phonon interactions. *Journal of Applied Physics 99*, 12 (2006), 123719.

[14] Klimeck, G., Boykin, T.B., Bowen, R.C., Lake, R., Blanks, D., Moise, T., Kao, Yung-Chung, and Frensley, W.R. Quantitative simulation of strained and unstrained inp-based resonant tunneling diodes. pp. 92–93.

[15] Kluksdahl, N. C., Kriman, A. M., Ferry, D. K., and Ringhofer, C. Self-consistent study of the resonant-tunneling diode. *Phys. Rev. B 39* (Apr. 1989), 7720–7735.

[16] Kohn, W., and Luttinger, J. M. Quantum theory of electrical transport phenomena. *Phys. Rev. 108*, 3 (Nov 1957), 590–611.

[17] Laux, S. E., Kumar, A., and Fischetti, M. V. Analysis of quantum ballistic electron transport in ultrasmall silicon devices including space-charge and geometric effects. *Journal of Applied Physics 95* (May 2004), 5545–5582.

[18] Laux, Steven E., and Stern, Frank. Electron states in narrow gate-induced channels in si. *Applied Physics Letters 49*, 2 (1986), 91–93.

[19] Lent, C. S., and Kirkner, D. J. The quantum transmitting boundary method. *Journal of Applied Physics 67* (May 1990), 6353–6359.

[20] Mahan, G. D. Quantum transport equation for electric and magnetic fields. *Physics Reports 145* (Jan. 1987), 251–318.

[21] Niceno, Bojan. A two-dimensional quality mesh generator. http://www-dinma.univ.trieste.it/nirftc/research/easymesh/easymesh.html.

[22] Potz, W. Self-consistent model of transport in quantum well tunneling structures. *Journal of Applied Physics 66*, 6 (1989), 2458–2466.

[23] Rammer, J., and Smith, H. Quantum field-theoretical methods in transport theory of metals. *Rev. Mod. Phys. 58*, 2 (Apr 1986), 323–359.

[24] Stratton, R. Diffusion of hot and cold electrons in semiconductor barriers. *Phys. Rev. 126*, 6 (Jun 1962), 2002–2014.

[25] Trellakis, A., Galick, A. T., Pacelli, A., and Ravaioli, U. Iteration scheme for the solution of the two-dimensional schrodinger-poisson equations in quantum structures. *Journal of Applied Physics 81*, 12 (1997), 7880–7884.

[26] van Hove, L. Quantum-mechanical perturbations giving rise to a statistical transport equation. *Physica 21* (1954), 517–540.

[27] van Wees, B. J., van Houten, H., Beenakker, C. W. J., Williamson, J. G., Kouwenhoven, L. P., van der Marel, D., and Foxon, C. T. Quantized conductance of point contacts in a two-dimensional electron gas. *Phys. Rev. Lett. 60*, 9 (Feb 1988), 848–850.

[28] Wigner, E. On the quantum correction for thermodynamic equilibrium. *Phys. Rev. 40*, 5 (Jun 1932), 749–759.